



Cite this: *Dalton Trans.*, 2025, **54**, 433

# Integration of metal–organic frameworks and clay toward functional composite materials

Anindita Chakraborty,<sup>a</sup> Jyoti<sup>a</sup> and Tapas Kumar Maji<sup>b,c</sup>

Metal–organic frameworks (MOFs) have become increasingly important as a class of porous crystalline materials because of their diverse applications. At the same time, significant progress has been achieved in the field of MOF-based composite materials toward novel applications based on the synergistic effect of two or more different components. Clay materials have been explored recently in MOF chemistry for the synthesis of MOF–clay composites, which are a new class of functional materials synthesized by a cooperative combination of MOFs with clay. Such composites have evolved only in the recent past with important functions and applications, such as enhanced gas storage and separation, CO<sub>2</sub> capture and conversion, catalysis, drug delivery, and water harvesting. Notably, the typical shortcomings of MOFs, such as moisture sensitivity, poor water dispersibility, poor thermal and chemical stability, and poor processability, could be overcome by developing novel MOF–clay composites. This article provides a concise overview of MOF–clay composites and their applications in various fields that will drive the interest of researchers to explore the emerging field of MOF–clay chemistry. In the initial sections, we classify the clays that have been used in MOF chemistry and briefly discuss their structures and chemistry. We also present the advantages of MOF–clay composites and discuss their synthetic methodologies. In the later sections, we classify different MOF–clay composites based on the clay and present some representative examples of such composites that show unique properties and applications. Finally, the development in this field is summarized, and the future scope of such composites is discussed.

Received 3rd October 2024,  
Accepted 13th November 2024

DOI: 10.1039/d4dt02789b

rsc.li/dalton

## 1. Introduction

Clays are materials that have played a significant role in human civilization from ancient times to current modern life and serve various industries like ceramics, plastics, and cosmetics. Typically, clay is defined by its fine mineral particles (<2 μm) mainly consisting of Al-based hydrous layered silicates, although it sometimes contains iron, alkali metals, or alkaline earth metals.<sup>1–3</sup> The exploration of clay, termed ‘clay science’ or ‘argillology’, gained traction in the mid-1930s when the ‘clay mineral concept’ was widely recognized.<sup>3</sup> Some of the naturally occurring clays are long known in history, such as pyrophyllite, talc, montmorillonite (MMT), saponite, palygorskite (PAL), sepiolite (SEP) and halloysite, and they have shown promise in catalysis, adsorption,<sup>4–7</sup> photocatalysis,<sup>8</sup> pharma-

ceutical and biomedical applications.<sup>9</sup> In recent times, following the emerging needs of civilization, chemists have developed a number of tailor-made synthetic clay materials, such as cloisite 30B, layered double hydroxide (LDH), laponite (LP) and aminoclay (AC),<sup>8,9,10–14</sup> which have shown exceptional potential in various fields such as catalysis,<sup>12,15–19</sup> biomedicine,<sup>10,11,13</sup> adsorption,<sup>20</sup> rheological studies,<sup>21</sup> drug delivery<sup>22</sup> and solubilizing insoluble dyes.<sup>23</sup> Clay materials have attracted widespread research interest and a number of research articles have been published on the synthesis, characterization and application of both natural and synthetic clays.<sup>4–14</sup>

Metal–organic frameworks (MOFs) are inorganic–organic hybrids that have emerged over the last few decades as novel functional materials.<sup>24–28</sup> The porous crystalline frameworks of MOFs are formed through the self-assembly of inorganic nodes and organic linkers.<sup>29,30</sup> The exceptional modularity and tunability of MOFs have prompted extensive exploration into their diverse applications like chemical sensing,<sup>31,32</sup> separation,<sup>33</sup> ion exchange,<sup>34</sup> drug delivery,<sup>35,36</sup> gas storage and release,<sup>29,37–39</sup> exclusion of harmful substances from the environment,<sup>40</sup> catalysis<sup>41–44</sup> and degradation of chemical warfare agents.<sup>45–47</sup> Despite their potential, MOFs have some shortcomings, such as inadequate thermal, chemical and mechanical stability, and poor processability, which eventually

<sup>a</sup>Department of Chemistry, School of Basic Sciences, Central University of Haryana, Mahendargarh 123031, Haryana, India. E-mail: achakraborty@cuh.ac.in

<sup>b</sup>New Chemistry Unit (NCU), Jawaharlal Nehru Centre for Advanced Scientific Research, Jakkur, Bangalore 560064, India

<sup>c</sup>Molecular Materials Laboratory, Chemistry and Physics of Materials Unit (CPMU), School of Advanced Materials (SAMat), International Centre for Materials Science, Jawaharlal Nehru Centre for Advanced Scientific Research, Jakkur, Bangalore 560064, India. E-mail: tmaji@jncasr.ac.in

limit their applicability. Hence, stability and processability stand as imperative necessities for exploring the potential use of MOF materials in desired applications and also for enhancing the scope of MOFs in practical fields. Thus, the current research goal is the development of new materials based on MOFs, which can meet the requirements of evolving fields without compromising the integrity of original MOFs, such as their crystalline nature and porosity. In this context, researchers have come up with a carefully crafted method that integrates MOFs with other functional materials. This approach opens the door for the creation of new superior MOF composites.<sup>48,49</sup> At present, numerous MOF hybrids have been reported, which are synthesized by integrating MOFs with various functional materials like graphene and graphene oxide,<sup>50,51</sup> silica,<sup>52</sup> carbon nanotubes,<sup>53</sup> quantum dots,<sup>54,55</sup> alumina,<sup>56</sup> metal oxides,<sup>57</sup> polymers,<sup>58</sup> metal nanoparticles/nanorods<sup>59</sup> and nanoclay (natural and synthetic).<sup>60–97</sup>

MOFs have been synergistically fused with a number of natural and synthetic clays, and such judicious fusion has resulted in the mitigation of the typical shortcomings of MOFs that have also exhibited novel properties and applications (Scheme 1). The functions and applications of MOF–clay composites range from enhanced gas adsorption and separation, CO<sub>2</sub> conversion, water harvesting, drug delivery, dye removal and degradation, chemical warfare agent simulants and catalysis.<sup>60–97</sup> Although explored only recently, MOF–clay composites represent an emerging field and we believe that these composites may take MOF research to the next level by advancing the scope and real applications of MOFs. Recently, we developed different highly processable MOF-based composites with AC and LP that showed enhanced CO<sub>2</sub> adsorption, separation, chemical fixation efficacy and atmospheric water harvesting compared to those of the individual components.<sup>86,87,90–94</sup> In this article, we have highlighted the synergistic approach for combining selected MOF and clay materials and how such combinations have resulted in desired functional composites. We first briefly introduce the classification and structure of clay materials with an emphasis on the

clays used in MOF chemistry (Schemes 2 and 3). We also present the advantages of MOF–clay composites over other contemporary functional materials and outline different synthetic methodologies to furnish these composites. In the subsequent sections, we categorize MOF–clay composites based on the types of clay used and discuss some representative examples. Finally, we summarize this emerging field and present a future outlook on the scope of these composites as next-generation MOF-based materials.

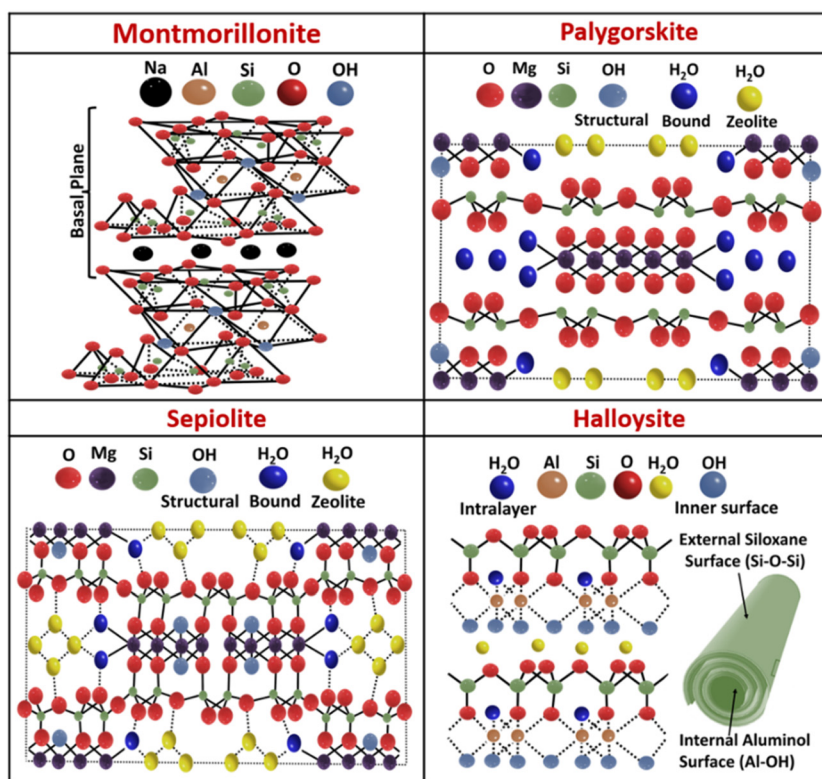
## 2. Brief introduction to clay materials: classifications and structures

For a long time, clay minerals have been known for their malleability, allowing them to be shaped when moist and then solidifying this shape upon drying or heating, provided it retains appropriate moisture levels. While clays are primarily composed of phyllosilicates, their additional constituents can influence their plasticity or hardening characteristics.<sup>2,3</sup> Clay minerals are mainly classified depending on the arrangement of their layer type and layer charge. Detailed discussions on their structure and classification are not part of the scope of this review but these can be found in the literature.<sup>1–4</sup> However, before discussing MOF–clay composites, we will present a brief overview of clay minerals to understand their general structures and types. In particular, we will discuss those specific clays that have served as crucial functional materials in novel MOF–clay composites.

Clays are mainly divided into two classes depending on the ratio of tetrahedral and octahedral layers, *i.e.*, 1 : 1 and 2 : 1. In the case of a 1 : 1 clay structure, one octahedral sheet aligns with one tetrahedral sheet.<sup>1–4</sup> On the other hand, in the case of a 2 : 1 clay structure, the basic unit of the clay layer contains one octahedral sheet that is enclosed between two tetrahedral sheets facing opposite directions. Further categorization of



**Scheme 1** Scheme showing MOF–clay composites and their diverse properties and applications. \*Different types of clay structures are presented in Schemes 2 and 3.



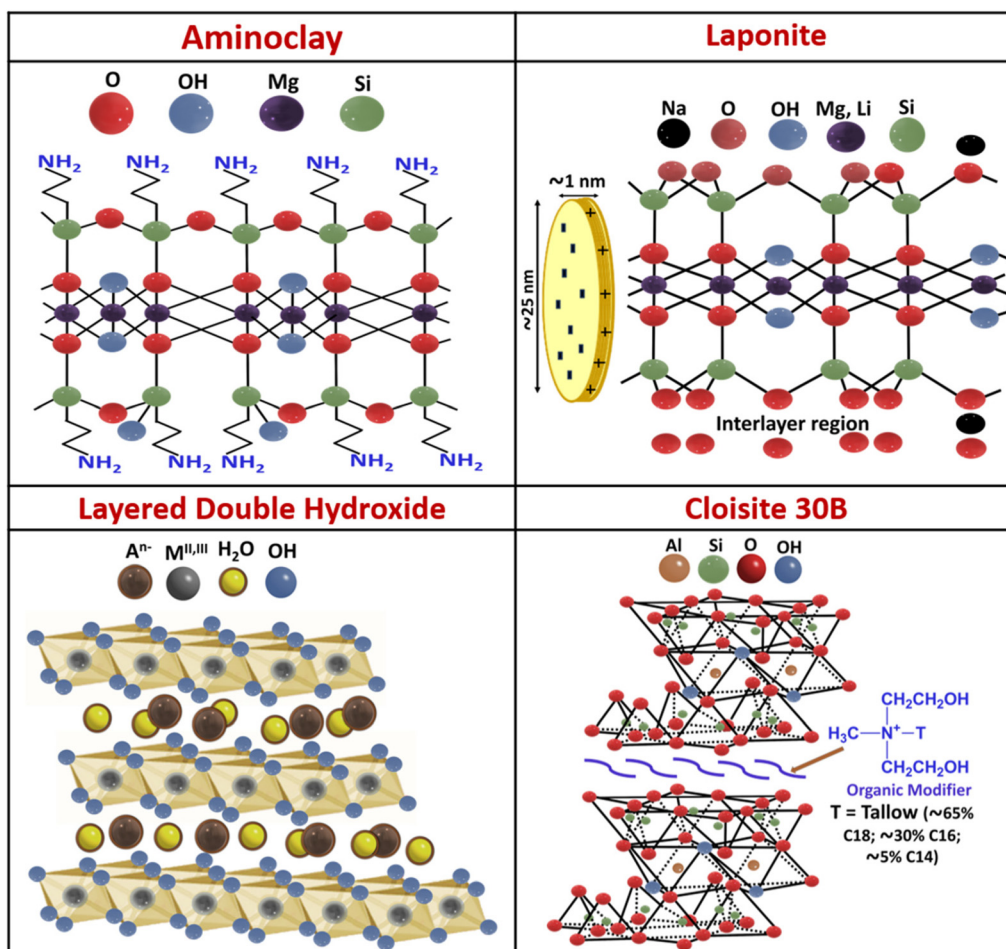
**Scheme 2** Structural representation of natural clays used in MOF chemistry.

clays involves considering the innate charge present in the clay's basal plane, which results from different substitutions present in the octahedral and tetrahedral sheets. According to the literature, clays have also been categorized as either natural or synthetic/modified clays. Generally, natural clays are commonly classified into three to four principal groups, namely montmorillonite-smectite, kaolinite, illite, and potentially chlorite. The kaolinite group encompasses minerals such as halloysite, kaolinite, dickite, and nacrite, whereas the montmorillonite-smectite group includes talc, pyrophyllite, saucornite, vermiculite, nontronite, saponite, and montmorillonite. The illite group primarily consists of clay minerals referred to as clay micas, with illite being the predominant mineral within this category.<sup>1–3</sup> Natural clays, despite their abundance, present notable drawbacks when compared to synthetic/modified clays. A major issue is their chemical variability depending on the source of extraction, which can lead to variations in their colour, texture and properties. Additionally, crystallographic imperfections stemming from their genesis and deposit location, along with the presence of impurities, pollutants, and poor dispersion in water (*i.e.*, smectite, kaolinite, and bentonites), limit their suitability for many important applications. This backdrop particularly hinders their use in fields that require precise chemical control, such as biomedicine.<sup>9</sup> In this regard, synthetic clays have shown promise, such as that through their enhanced water dispersibility, which is essential for many biological and catalytic applications.<sup>10–19</sup>

Such promising properties and applications of clays have also been achieved in MOF-clay composites, with additional features originating from the MOF counterpart.<sup>60–97</sup> Schemes 2 and 3 present brief structural overviews of clays that have been used in MOF chemistry. Illustrative examples of selected clays and their MOF composites are discussed in section 4.

### 3. MOF-clay composites: advantages over other materials and synthetic methodologies

Over the years, MOF research has translated synthesizing new MOFs and expanding their family to fabricating new MOF-based functional materials. After realizing that MOF composites could enhance the scope of MOFs many fold, chemists escalated research on MOF composites, which has primarily evolved over the last decade.<sup>48,51,98</sup> In the design of MOF composites, the choice of other functional materials is crucial as this ultimately directs the microstructures, properties and applications of the resulting hybrids. Literature surveys on emergent MOF-clay composites clearly suggest that clays offer unique advantages for uplifting the properties and applications of MOFs. Certain aspects give MOF-clay composites an edge over the pristine parent materials (MOFs and clay) and other contemporary porous composites, such as:



**Scheme 3** Structural representation of synthetic clays used in MOF chemistry.

1. A suitably functional clay can undergo distinctive cooperative interaction with selected MOFs and such cooperativity enhances the properties of the composites, making them ideal for gas storage and separation, CO<sub>2</sub> fixation and conversion, catalysis, drug delivery and water harvesting.<sup>86–97</sup> The resulting hybrids often show enhanced properties compared to those of the parent MOFs or clay; and sometimes introduction of a completely new property can be possible.

2. Many natural clays are abundant and environment friendly, while a good number of synthetic clays are inexpensive and easy to synthesize. Their abundance and cost-effectiveness are advantageous while we choose clay as one of the parent materials in MOF composites. This is in contrast to other functional materials such as metal nanoparticles or quantum dots that have been used in MOF chemistry to make composites.

3. Some synthetic clays, such as AC,<sup>99,100</sup> offer diverse opportunities to functionalize their 2D nanosheets. Such functionalization supports MOF nucleation and growth by offering unique interactions between the MOF building blocks and the functionalized clay surface.

4. The high thermal stability and robust structure of clays are expected to enhance the stability (thermal and mechanical) of the resulting MOF composites.<sup>62,68,69,95</sup>

5. The high water dispersibility of certain synthetic clays (e.g., AC and LP) offers a unique opportunity to fabricate water-dispersible MOF composites<sup>86,90</sup> using MOFs that are mostly insoluble and non-dispersible in the majority of solvents, including water. Such water dispersibility of these composites is promising for their practical applications, such as making membranes for devices and biological applications.

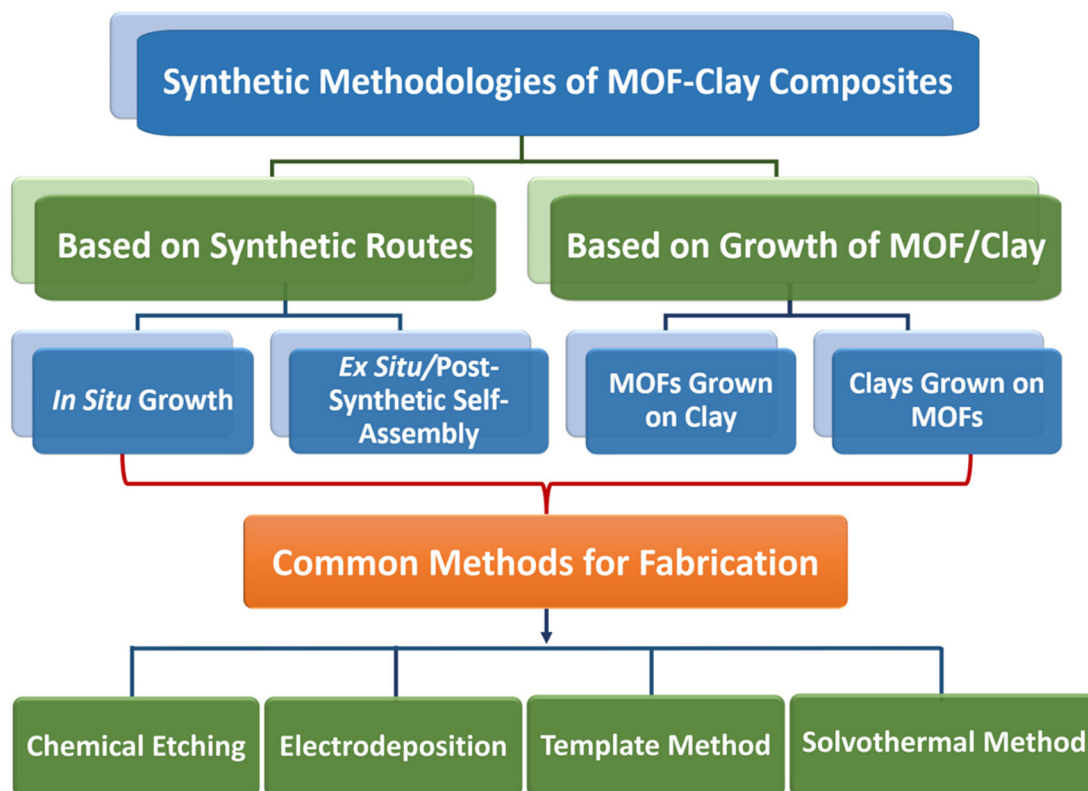
The cooperativity in a composite originates from the interaction of the MOF's nodes and linkers with the clay and hence the choice of parent materials is crucial for the design of these composites. While the parent design has to be done thoughtfully, the formation of composites is often serendipitous, occurring by self-assembly reactions under certain conditions and it is difficult to predict the exact microstructure/morphology and properties of the composites. However, by applying knowledge of synthetic and supramolecular chemistry, judicious approaches have been adopted to synthesize various MOF-clay composites. Broadly, the synthesis of MOF-clay composites (Scheme 4) can be cate-



gorized into two primary methods: *in situ* growth of the composites<sup>62–66,68–75,77,78,80–83,90–94,96,101–103</sup> and an *ex situ* process involving post-synthetic modification.<sup>60,61,67,76,79,84,86–89,95,97</sup> In the case of the *in situ* method, MOF precursors are added to the clay component and the composite forms in a single-step (one-pot) process; meanwhile, the *ex situ* method involves the interaction of a pre-synthesized MOF with its clay counterpart. The *in situ* method has been widely adopted to develop well-integrated composites and a notable example is the synthesis of CuBTC@AC composites, where amine-functionalized AC sheets stabilize Cu<sup>2+</sup> ions, preventing their aggregation and facilitating the formation of ultra-small CuBTC nanoparticles on the AC surface.<sup>90</sup> Other representative examples include the *in situ* growth of Ru-MOFs on MMT using a solvothermal method,<sup>62</sup> and the synthesis of UiO-66/PAL composites *via* a one-pot process.<sup>73</sup> Fabrication of new core-shell MOF structures has also been possible by the *in situ* approach, although the process is often serendipitous.<sup>63,96,101–103</sup> A few typical examples include the core-shell Fe<sub>3</sub>O<sub>4</sub>@AC-NH<sub>2</sub>@Cu-opa composite<sup>96</sup> and the core-shell drug@M-ZIF-8 nanosystem.<sup>63</sup> The details of synthetic pathways of such core-shell composites along with their features are also discussed in section 4. The *ex situ* approach is relatively less frequently observed, but has been found to be effective in furnishing novel composites with targeted microstructures and properties. An example

of this technique includes the coating of preformed ZIF-8 MOF nanoparticles with layers of LP clay for the targeted fabrication of a hydrogel nanocomposite exhibiting controlled delivery of drug molecules.<sup>86</sup> Using an *ex situ* method, Co-based spinel nanocrystals have also been assembled on ZIF-67 frameworks to form the LP@ZIF-67 composite.<sup>89</sup>

Synthetic routes to MOF-clay composites may also be classified based on the growth of one component on the other. There are two categories where (i) MOFs are grown on the clay surface<sup>62,70,72–75,78,81–83,90,104</sup> and (ii) clays are grown on MOFs.<sup>79,105–108</sup> In cases where MOFs are grown on clay, the hydrothermal/solvothermal method is commonly employed, promoting strong interactions between the clay surface and the MOFs.<sup>70,72,78,90</sup> For example, the MIL-53(Al)@AC nanocomposite is synthesized *via* a hydrothermal method where the MIL-53(Al) MOF is grown on the AC surface.<sup>95</sup> The template method is sometimes employed to grow MOFs on the clay surface, resulting in hollow MOF structures. A representative example is the formation of a composite in which ZIF-8 nanocrystals are grown onto H-LDH, yielding the successful fabrication of H-LDH@ZIF-8.<sup>104</sup> Conversely, growing clay on the surfaces of MOFs is a less common approach and to the best of our knowledge, this approach is primarily limited to growing LDHs on MOFs.<sup>105–108</sup> Representative examples include the synthesis of a novel NiFe-LDH@Ni-MOF/NF hetero-structured electrocatalyst<sup>105</sup> and core-shell Co-HKUST@CoMn-



**Scheme 4** Schematic representation of the synthetic methodologies of MOF-clay composites.

LDH composites<sup>108</sup> by the electrodeposition method and fabrication of the HCSs@Mn/Co-LDH composite by the chemical etching method.<sup>107</sup>

## 4. MOF–clay composites based on different types of clays

Among different types of nanoclays (natural and synthetic), there are a few clays that have shown promise in MOF–clay chemistry. Natural clays include halloysite, MMT, SEP and PAL, while synthetic clays are LDH, cloisite 30B, AC and LP (Schemes 2 and 3). Halloysite, a natural clay mineral, has a tubular structure with inner surfaces carrying positive charges due to aluminium hydroxide and outer surfaces bearing negative charges from siloxane groups. Under highly acidic conditions, its outer surfaces can become positively charged. These surface properties are key for applications in various fields like drug delivery, catalysis and tissue engineering.<sup>9</sup> Only a few halloysite–MOF composites are known, and these have shown promise in catalysis,<sup>74,75</sup> flame retardancy,<sup>76</sup> and adsorption.<sup>77</sup> Cloisite 30B is a modified MMT clay synthesized by the exchange of Na<sup>+</sup> ions present in MMT with an organic modifier. A 3D printing strategy was employed to construct a hierarchical porous framework of MOF–cloisite composites for the quick and highly efficient removal of dye from wastewater, as reported by Rahimi and co-workers.<sup>78</sup> LDHs are anionic lamellar chemical compounds that contain cationic brucite-like sheets,<sup>8,9</sup> which are stabilized by charge-balancing anions and interlayer water molecules. The LDH–MOF composites reviewed in the literature<sup>85</sup> show promise as supercapacitors,<sup>79,80</sup> in water remediation systems,<sup>81–84</sup> and as energy storage and environmental devices.<sup>109</sup> In this article, we have limited our discussion to MOF composites with some important clays such as MMT, SEP, PAL, LP and AC. In the following sections, we present some representative examples of such composites, which may emerge as next-generation MOF-based materials with desired functions and applications.

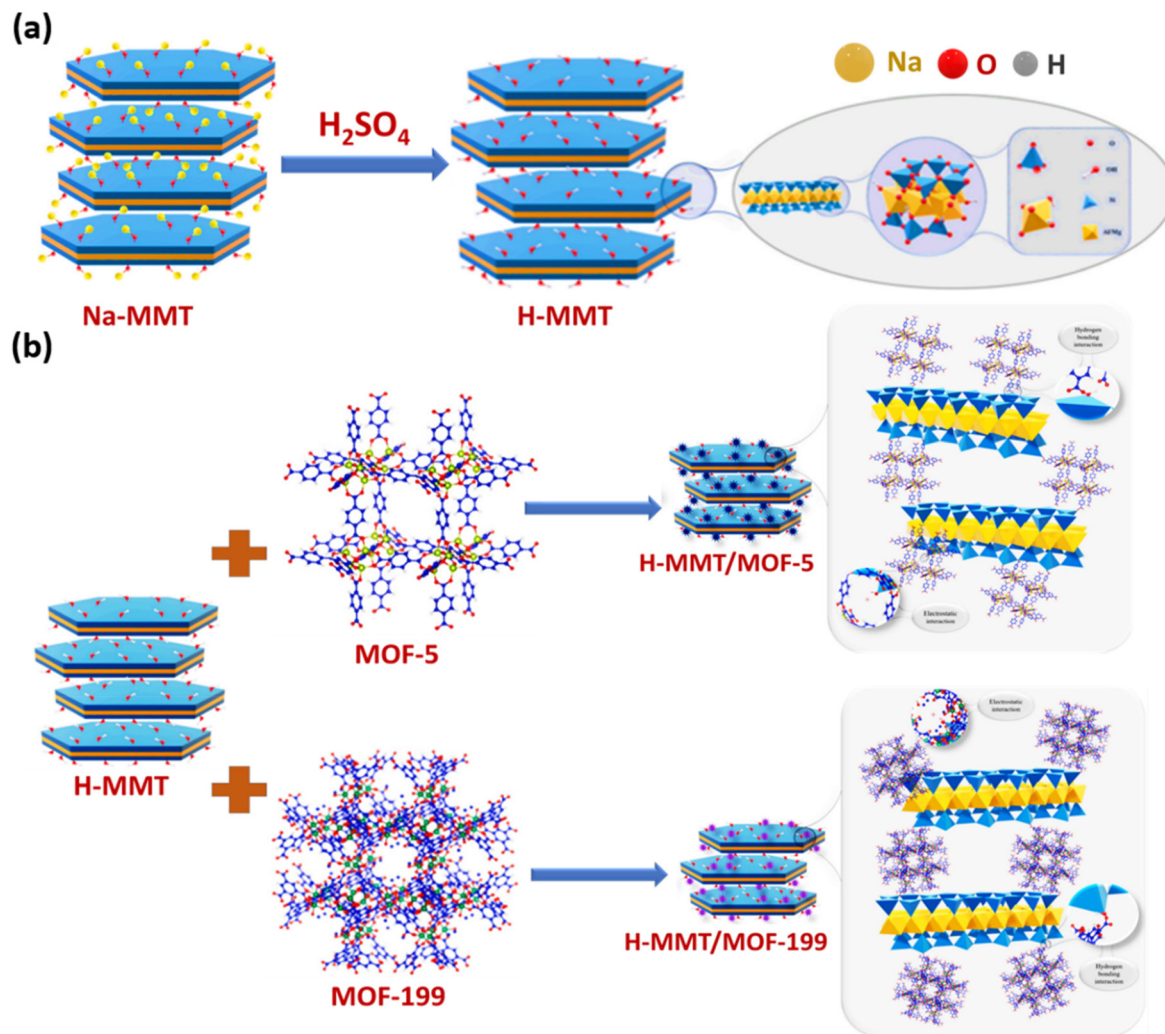
### 4.1. MOF–montmorillonite composites

MMT is an extensively studied natural clay because of its abundance and cost-effectiveness. It is characterized by a 2:1 layered framework comprising an octahedral alumina sheet flanked by two inward-pointing tetrahedral silica layers having a common formula (Na, Ca)<sub>0.33</sub>(Al, Mg)<sub>2</sub>(Si<sub>4</sub>O<sub>10</sub>)(OH)<sub>2</sub>·*n*H<sub>2</sub>O (Scheme 2).<sup>2–5,9</sup> MMT/MOF composites have shown great promise in various applications, including water remediation, drug delivery, improvement in the wear resistance of resins, and catalysis.<sup>60–66</sup> Inspired by the natural adsorbent properties of clays and further exploiting the porosity of MOFs, Shariatnia *et al.*<sup>60</sup> explored the effectiveness of natural clay-based MOF composites such as H-MMT/MOF-5 and H-MMT/MOF-199 as highly effective adsorbents for the removal of methylene blue dye (MB). Na<sup>+</sup>–MMT clay was first transformed into activated H-MMT by treating it with a strong acid, H<sub>2</sub>SO<sub>4</sub> (Scheme 5). By acid treatment, the porosity of the clay was

enhanced, resulting in an increase in its dye uptake ability compared to that of the Na<sup>+</sup>–MMT. The clay mineral H-MMT, known for its larger specific surface area (SSA) and reactive OH groups, was identified as an excellent candidate for furnishing a cost-effective and environmentally friendly composite adsorbent. Subsequently, the authors reported various composites of H-MMT/MOF-5 and H-MMT/MOF-199 (Scheme 5) having enhanced adsorption capacity compared to that of H-MMT. PXRD patterns of all the synthesized materials, including H-MMT, MOF-5, H-MMT/MOF-5, MOF-199, and H-MMT/MOF-199 indicated the effective formation of the H-MMT/MOF-5 composite. The surface morphology of MOF-5 revealed well-defined cubic particles with a smooth surface, while the H<sub>2</sub>SO<sub>4</sub>-modified H-MMT clay exhibited substantial plate aggregates with a sheet-like structure. FESEM images of H-MMT/MOF-5 showed that MOF-5 particles are distributed between and on the surface of the H-MMT layer. MOF-199 displayed polyhedral particles with defined edges and a clear porous structure, indicative of high crystallinity.

The morphology of H-MMT/MOF-199 depicted particles dispersed between and on the surface of H-MMT sheets. Following the adsorption of MB onto the H-MMT/MOF-5 and H-MMT/MOF-199 surfaces, SEM micrographs showed agglomerations in specific regions resulting from interactions among the mixed particles. The anions present on the solid surface of the adsorbent can attract positively charged dye ions in the MB solution, leading to the aggregation of adsorbent particles. Moreover, after adsorption, the surface became smoother and more uniform, indicating slight alterations in the adsorbent surfaces caused by the dye molecules. Thermodynamic experiments revealed that at temperatures ranging from 283 to 313 K, when H-MMT/MOF-5 and H-MMT/MOF-199 were used, all reactions were spontaneous and exothermic. The mechanisms of MB adsorption by the H-MMT/MOF-5 and H-MMT/MOF-199 composites were attributed to the creation of H-bonds, electrostatic attraction, and  $\pi$ – $\pi$  interactions. Optimal MB removal efficiencies of 97.52% and 98.73% were achieved for the 60% H-MMT/40% MOF-5 and 70% H-MMT/30% MOF-199 composites, respectively, with corresponding maximum adsorption capacities ( $q_{\text{max}}$ ) of 192.3 mg g<sup>−1</sup> and 238.09 mg g<sup>−1</sup>. Comparison between H-MMT, H-MMT/MOF-5, and H-MMT/MOF-199 demonstrated that H-MMT/MOF-199 was the most effective adsorbent, as it exhibited a higher  $q_{\text{max}}$  value and a larger surface area.

Zhang *et al.* explored the advancement of durable PBO (poly(*p*-phenylene benzobisoxazole)) fabric composites by adding Co-MOF nanosheets and OMMT (modified MMT).<sup>61</sup> Co-MOF nanosheets were deposited at the interface of the PBO fabric *via* coordination interactions to enhance surface properties such as roughness and compatibility of the PBO fabric, which significantly enhanced the interfacial adhesion at the interface of the composites. FESEM images (Fig. 1) revealed that the surface of pure PBO fibers was extremely uniform and smooth. Also, PBO fibers were uniformly coated with the nanosheets, enabling the phenolic resin to infiltrate the loose structures and form strong mechanical interlocking between



**Scheme 5** Schematic representation of (a) formation of the modified H-MMT structure and (b) possible interactions of H-MMT occurring with MOF-5 or MOF-199. This figure has been adapted from ref. 60 with permission from Elsevier, copyright 2023.

the PBO fibers and the matrix. Elemental mapping images (Fig. 1) of the Co-MOF@PBO fabric showed homogeneous distribution of C, O, and Co elements across the fiber surfaces, indicating well-distributed deposition of the Co-MOF onto the fibers. OMMT, with expansive layer spacing, tends to slip between its layers, facilitating its dispersion within the resin matrix. This dispersion aids in forming a transfer film on the contact surface and promotes physical entanglement with resin chains, enhancing the composite's mechanical properties. It also enhanced the compatibility with the resin and its larger layered structure, resulting in better durability. The research found that Co-MOF@PBO/OMMT composites showed excellent wear-resisting ability due to the mutual effect of the modified Co-MOF interface and OMMT reinforcement. The study emphasized the significance of interfaces and reinforcement in boosting the resistance to abrasion in fabric composites. Moreover, tribological tests were carried out on a pin-on-disc tester to show how the OMMT filler influences tribological behaviour. The results

demonstrated that the composite with the addition of 2 wt% of OMMT filler presented excellent anti-wear resistance and the wear rate was reduced by 19.1% compared to the composite without the addition of filler.

Miao *et al.*<sup>62</sup> presented the catalytic properties of a novel MMT/MOF composite material, Ru-MOF\_MMT, which consists of Ru-MOFs  $[Ru_2^{II,III}(BTC)_2X_xY_{1.5-x}]$  (where, BTC = 1,3,5-benzenetricarboxylate, X, Y =  $Cl^-$  or  $OH^-$ ) grown on MMT (Scheme 6). This composite was synthesized through an *in situ* solvothermal reaction that significantly enhanced its surface area, thereby boosting its catalytic capabilities. After the synthesis of the composite, the material underwent an annealing process that disrupted the Ru-MOF structure, creating coordinatively unsaturated sites (CUS) essential for catalytic activity. The  $N_2$  adsorption-desorption isotherms of all the samples, *i.e.*, MMT, Ru-MOF\_MMT and Ru\_MMT showed a large specific surface area ( $265\text{ m}^2\text{ g}^{-1}$ ) of the composite as compared to that of the other materials due to the presence of CUS in the structure. The Ru-MOF\_MMT composite exhibited



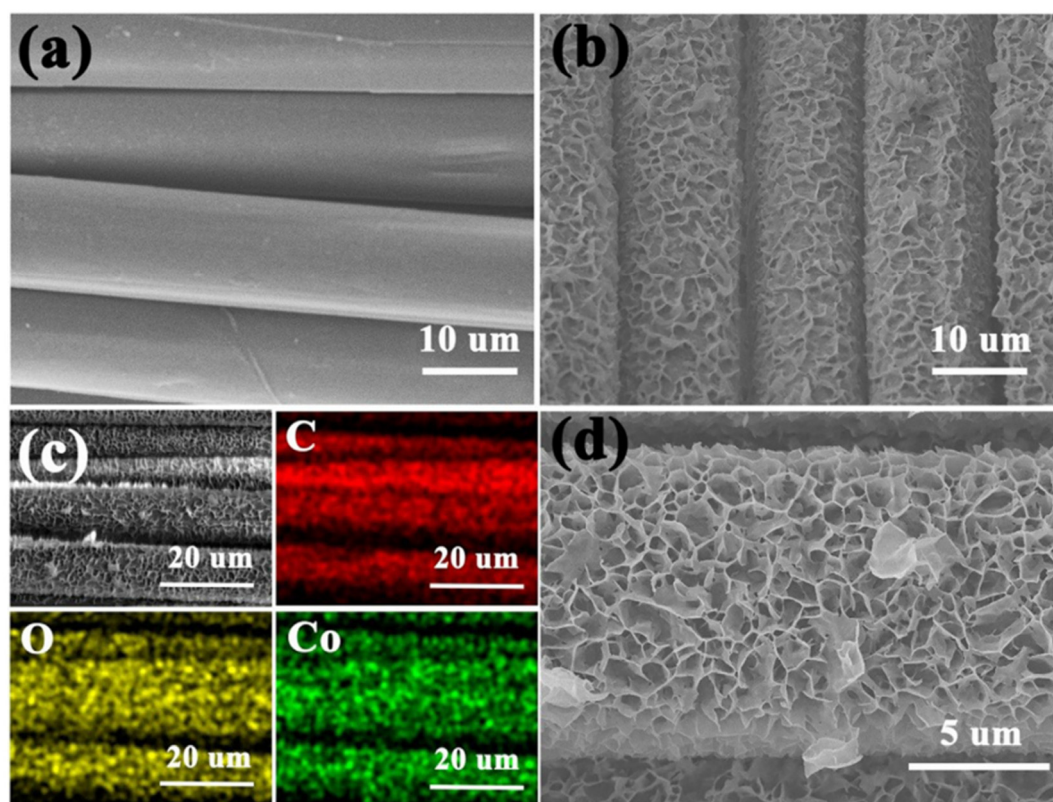
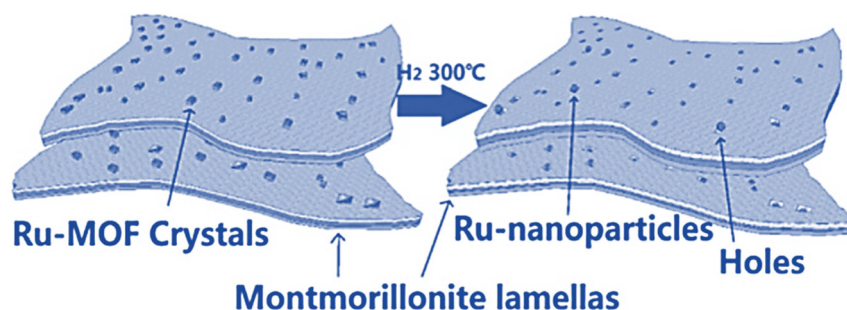


**Fig. 1** FESEM images of (a) pure PBO fabric, and (b) and (d) Co-MOF nanosheets anchored onto the fabric, and (c) elemental mapping of Co-MOF@PBO fibers showing uniform distribution of all the elements. This figure has been adapted from ref. 61 with permission from Elsevier, copyright 2022.



**Scheme 6** Schematic representation of the *in situ* growth of the Ru-MOF on the surfaces of MMT and the Ru nano-clusters developed after  $H_2$  annealing at 300 °C. This figure has been adapted from ref. 62 with permission from Elsevier, copyright 2016.

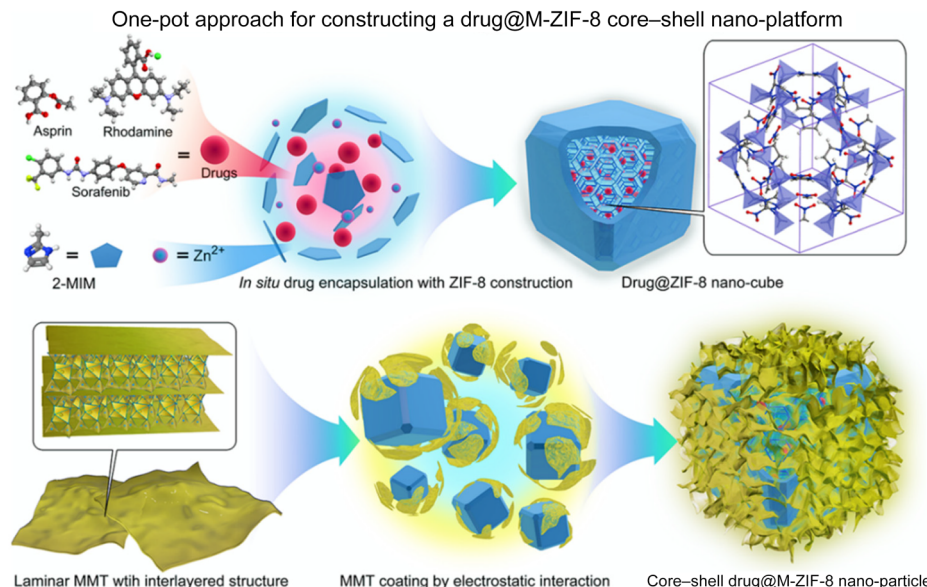
exceptional efficiency in catalyzing benzene hydrogenation, achieving a high turnover frequency (TOF) of  $3478 \text{ h}^{-1}$ . The catalyst demonstrated remarkable stability, maintaining its activity over at least five cycles without any degradation of the catalyst.

Bai *et al.*<sup>63</sup> discussed the development of a new core-shell nanosystem for drug delivery named drug@M-ZIF-8. The development of drug@M-ZIF-8 involved a process where drugs were encapsulated within ZIF-8 and then coated with MMT (M) to form a core-shell nanoplateform. The authors explored the drug encapsulation in ZIF-8 by one-pot synthesis using three

different types of nonsteroidal anti-inflammatory drugs (NSAIDs) such as rhodamine (Rho), sorafenib (Sor) and aspirin (Asp), denoted as drug@ZIF-8 (Rho@ZIF-8, Sor@ZIF-8 and Asp@ZIF-8) (Scheme 7).

The uniform capping of MMT over drug@ZIF-8 was processed by the electrostatic interaction present in the system. M-ZIF-8 had the potential to deliver NSAIDs to reduce inflammation without causing irritation in the gastrointestinal (GI) tract and promoting the healing of mucosal tissues. The controlled release of drugs extended GI retention and reduced toxicity. Testing in both gastritis and colitis models confirmed





**Scheme 7** Schematic diagram of the successive one-pot synthesis of the drug@M-ZIF-8 nanosystem. This figure has been adapted from ref. 63 with permission from the American Chemical Society, copyright 2020.

the effects of M-ZIF 8 on drug delivery and mucosal improvement.

#### 4.2. MOF-sepiolite/palygorskite composites

Fibrous natural clays SEP and PAL are composed of magnesium hydrosilicate, belonging to the group of silicates. SEP has an ideal formula of  $\text{Si}_{12}\text{Mg}_8\text{O}_{30}(\text{OH})_4(\text{H}_2\text{O})_4 \cdot 8\text{H}_2\text{O}$ , while PAL has an ideal formula of  $\text{Si}_8\text{Mg}_5\text{O}_{20}(\text{OH})_2(\text{H}_2\text{O})_4 \cdot 4\text{H}_2\text{O}$ . Both clay minerals (SEP and PAL) exhibit similar structures, with tetrahedral units facing the same direction, forming a 2:1 ribbon extending along the *a*-axis direction (Scheme 2). The potential use of SEP and PAL clays by integrating them with MOFs has been explored to overcome the drawbacks of MOFs for various practical applications such as gas storage/separation, adsorption, catalysis and environmental remediation,<sup>67–73</sup> and we discuss a few representative composites here.

Zhang *et al.*<sup>67</sup> reported an inventive method for enhancing the flame retardancy of thermoplastic polyurethane (TPU) by incorporating a hybrid material comprising a combination of a prototype MOF (ZIF-8) and SEP clay. FTIR and PXRD techniques were employed to verify the existence of characteristic peaks and lattices associated with ZIF-8 and SEP, affirming the successful synthesis of the hybrid. FESEM and EDS offered insights into the microtopography and elemental composition, revealing a rough surface and the presence of Si, Mg, Zn, and N elements (Fig. 2). The study illustrated that the synergistic flame retardant, ZIF-8@SEP, not only improved the limiting oxygen index (LOI) and flammability performance (UL-94V-0 grade rating of TPU), but also significantly reduced both the heat release rate and total heat release, thus contributing to a safer material with reduced fire hazards. Additionally, the novel flame retardant effectively absorbed

smoke, mitigating the increased smoke production typically caused by aluminium hypophosphite (AHP). Notably, the integration of ZIF-8@SEP in TPU composites has minimal impact on the material's tensile strength and elongation at break, ensuring the preservation of its mechanical integrity.

Pawar and co-workers<sup>68</sup> synthesized novel MOF-clay composite materials by an *in situ* method, denoted as MOF@SEP<sub>*n*</sub> (*n* = 1–4), by precipitating a stable MOF,  $\{\text{Zr}_6\text{O}_4(\text{OH})_4(\text{ABDC})_6\}$  (where ABDC = 2-aminobenzene-1,4-dicarboxylic acid), onto the natural clay SEP. Among all the composites, MOF@SEP<sub>3</sub> showed better N<sub>2</sub> adsorption at low pressure than the parent MOF and the clay material. FESEM images demonstrated that the parent MOF particles were finely dispersed on the surface of the SEP clay. The composites exhibited enhanced thermal stability as the loading of the clay mineral increased. In the presence of visible light irradiation, the MOF@SEP<sub>3</sub> composite showed efficient adsorption due to the synergy present in the MOF@SEP<sub>3</sub> composite. These composites were also employed as photocatalysts for the degradation of organic dyes in aqueous solutions, and the MOF@SEP<sub>3</sub> composite was found to be more effective for photocatalysis.

Wang *et al.*<sup>69</sup> developed PAL/MIL 88A(Fe) composites (PMFe-*x*, *x* is the added amount of Fe(III) salt in mmol) to remove Congo red dye in water treatment. Integrating PAL into MIL-88A(Fe) composites through an *in situ* growth method by using different amounts (2, 6, 10, 14 and 18 mmol) of Fe(III) salt resulted in an enhancement in stability and adsorption capabilities in the case of the PMFe-10 composite. The PXRD pattern of all the samples revealed that the pure phase of MIL-88A was present in the composite. SEM images of the samples showed the successful formation of composites with an increase in the roughness on the surface due to the presence of PAL content (Fig. 3).

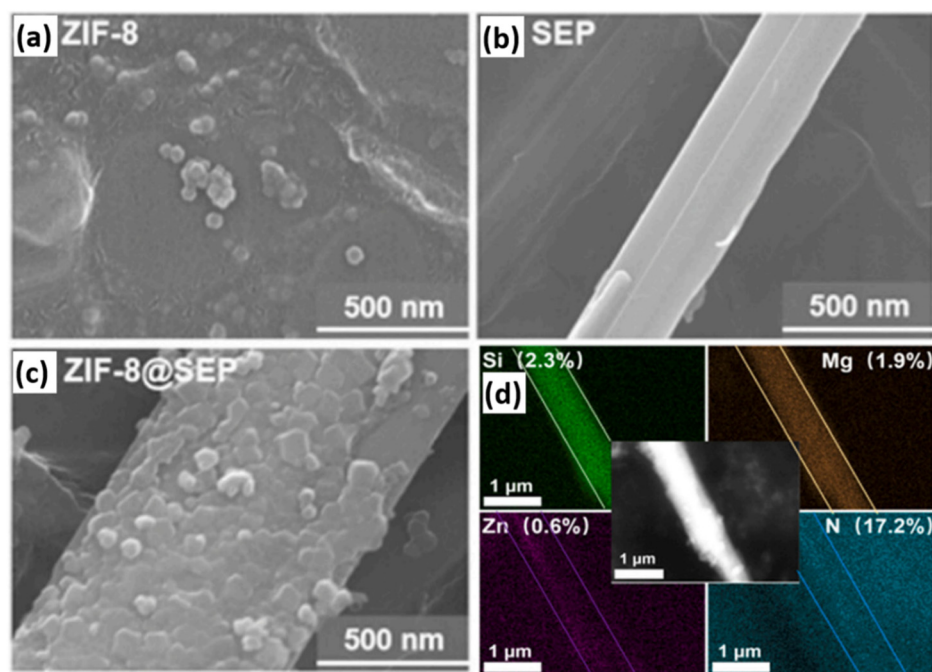


Fig. 2 SEM images of (a) ZIF-8, (b) SEP, and (c) ZIF-8@SEP. (d) EDS spectrum of ZIF-8@SEP. This figure has been adapted from ref. 67 with permission from Elsevier, copyright 2021.

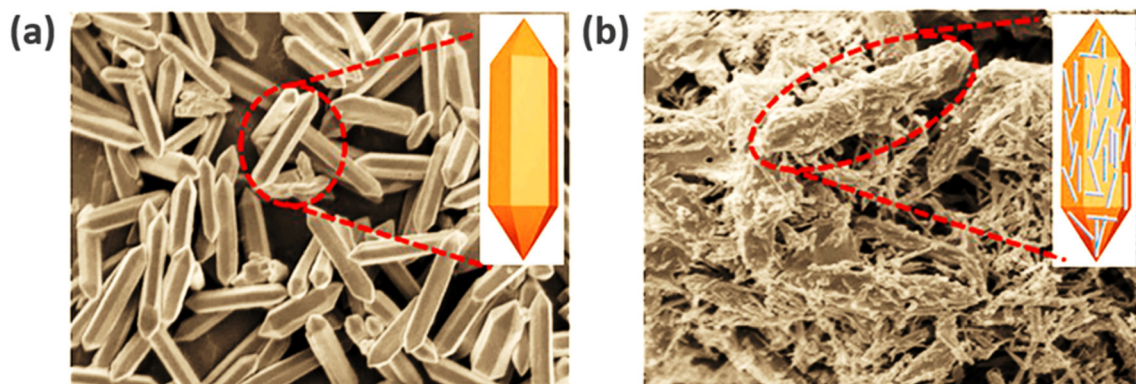


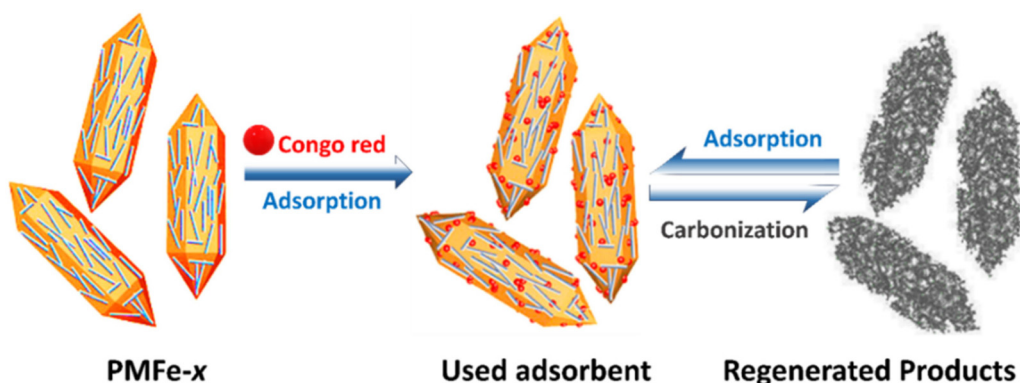
Fig. 3 FESEM images of (a) MIL-88A(Fe) and (b) PMFe-x. This figure has been adapted from ref. 69 with permission from Elsevier, copyright 2023.

The PMFe-10 composite showed absorption efficiency and acid/alkali resistance at various pH levels, achieving a maximum adsorption capacity of  $1141.4 \text{ mg g}^{-1}$  for Congo red in only 3 hours. In addition to this, the composite also showed efficient regeneration and reusability over five cycles by using one-step pyrolysis carbonization (Scheme 8). The mechanisms behind the adsorption of Congo red by the composites involved H-bonding interaction, electrostatic attraction and coordination effects.

#### 4.3. MOF-laponite composites

LP is a tailor-made clay mineral that bears a striking resemblance to hectorite clay (a naturally occurring clay). Both LP and hectorite are phyllosilicates that belong to the smectite

group, characterized by a unique 2:1 crystal structure made up of stacked units containing two sheets of tetrahedral silica surrounding an octahedral sheet that contains one  $\text{Mg}^{2+}$  cation.<sup>10,11</sup> The microstructure of LP can be represented as anisotropic disks having particle diameters of approximately 25 nm and a width of less than 1 nm (Scheme 3). Its chemical composition,  $\text{Na}^{+}_{0.7}[(\text{Si}_8\text{Mg}_{5.5}\text{Li}_{0.3})\text{O}_{20}(\text{OH})_4]^{-0.7}$ , suggests the presence of positively charged lithium ions substituting for magnesium ions in its framework. Recently, a number of novel nanocomposite materials based on LP have shown promise, thanks to their high water dispersibility and the remarkable rheological properties of LP.<sup>21,110,111</sup> In an aqueous medium, the delamination of LP nanosheets into a single nanosheet enhances the surface area, thereby enhancing the interaction

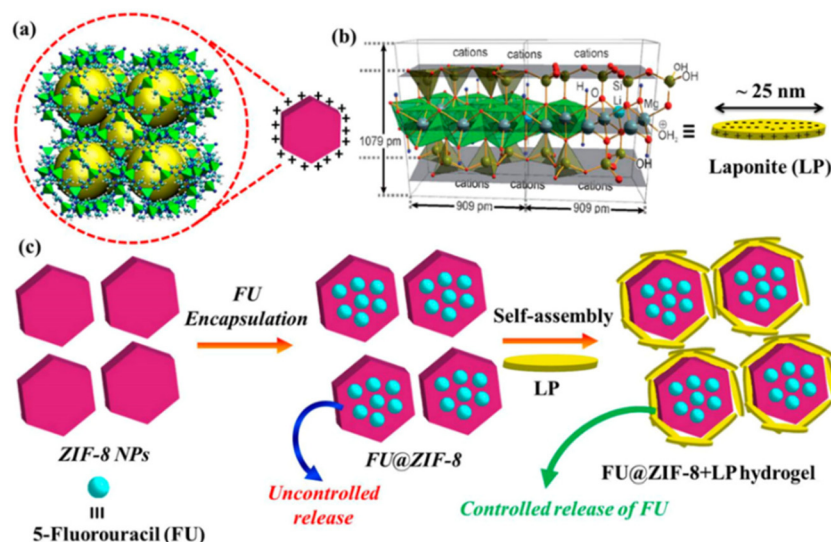


**Scheme 8** Adsorption of Congo red using PMFe-x composites and the carbonization regeneration cycling process. This figure has been adapted from ref. 69 with permission from Elsevier, copyright 2023.

with biomolecules. Apart from their use in biomedicine, remarkable features and applications, such as fabrication of shape-persistent modifiable hydrogels,<sup>111</sup> targeted drug delivery<sup>10,11</sup> or solubilizing an insoluble dye,<sup>2,3</sup> could also be achieved by judiciously synthesizing LP composites. Despite the great promise of LP to furnish functional nanocomposites, its exploration in MOF chemistry is limited. Our group envisaged that the self-assembly of MOF NPs with LP would be an interesting field to pursue, targeting nanocomposite hydrogels with enhancement in solution processability, high mechanical/thermal stability, and stimuli-responsive behaviour. However, it may be noted that the fabrication of a soft gel material from a hard MOF material is not an easy task. Strategies such as cross-linking of organic polymers with MOFs<sup>112,113</sup> or conversion of surface-anchored MOFs<sup>114</sup> have been adopted to furnish MOF-derived gels, which often involve tedious synthetic processes. Self-assembly of MOF NPs with LP paved the way for facile and easy fabrication of MOF-based

hydrogel nanocomposites of ZIF-8 and LP nanoclay.<sup>86</sup> Employing a charge-assisted self-assembly method, we successfully coated the positively charged surfaces of ZIF-8 NPs with LP, known for its negatively charged facets, resulting in the formation of a ZIF-8 + LP hydrogel nanocomposite. Our study also highlighted the controlled release of 5-fluorouracil (FU) from a hydrogel composite encapsulating FU-loaded ZIF-8 (FU@ZIF-8 + LP) (Scheme 9). Additionally, we demonstrated the formation of a fluorescent hydrogel by initially encapsulating the fluorescent “drug mimic” fluorescein within ZIF-8, followed by gelation with LP.

TEM images showed that the LP layers coated the surface of hexagonal ZIF-8 NPs in a ZIF-8 + LP xerogel as a consequence of the strong interaction between the unsaturated Zn<sup>2+</sup> sites on the surface of ZIF-8 NPs and the negatively charged faces of LP. Rheological analysis confirmed the viscoelastic nature of the ZIF-8 + LP hydrogel, with the storage modulus ( $G'$ ) surpassing the loss modulus ( $G''$ ) (Fig. 4).



**Scheme 9** Schematic illustration of (a) the structure of ZIF-8, (b) the structure of LP, and (c) the self-assembly of ZIF-8 and LP NPs toward nanocomposite gel formation. This figure has been adapted from ref. 86 with permission from the American Chemical Society, copyright 2018.



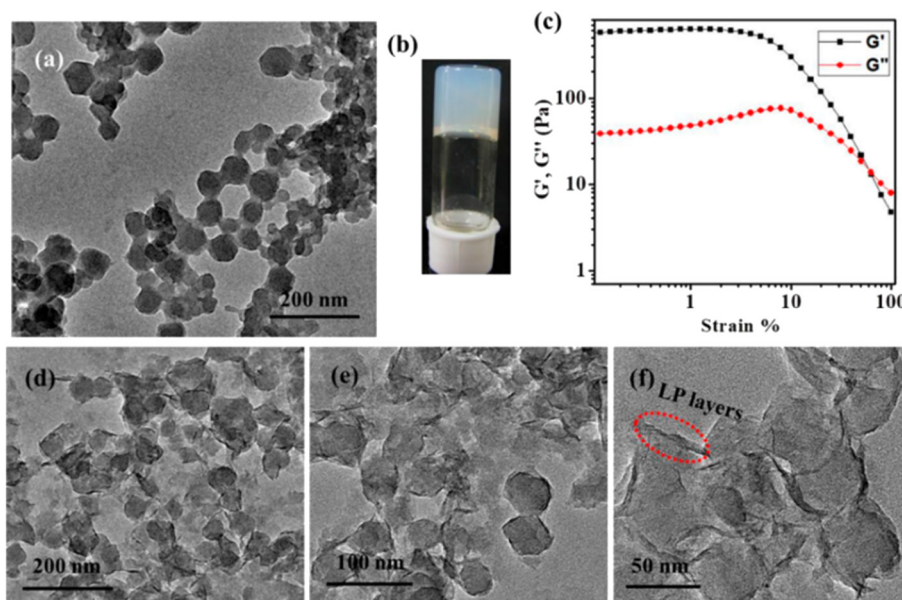


**Fig. 4** (a) TEM image of the ZIF-8 NPs, (b) image of the ZIF-8 + LP hydrogel, (c) strain measurements of the ZIF-8 + LP hydrogel: black squares, storage modulus ( $G'$ ); red squares, loss modulus ( $G''$ ). (d–f) TEM images of the ZIF-8 + LP xerogel. This figure has been adapted from ref. 86 with permission from the American Chemical Society, copyright 2018.

By employing a one-pot synthesis technique, we embedded the fluorescein dye molecule within ZIF-8 NPs, resulting in the formation of fluorescein@ZIF-8. Gelation performed using LP and fluorescein@ZIF-8 produced the hydrogel composite, fluorescein@ZIF-8 + LP, which displayed an intense radiant bright-green emission, arising from the embedded dye. The hydrogel exhibited a lifetime and a quantum yield of 3.8 ns and 86%, respectively. Moreover, the composite demonstrated superior processability, allowing for easy application onto a glass substrate without compromising its emission properties. The encapsulation of the small-molecule anticancer drug 5-fluorouracil (FU) into porous ZIF-8 and subsequent gelation of the FU@ZIF-8 material with LP yielded a stable hydrogel composite FU@ZIF-8 + LP, which exhibited a finely tuned pH-responsive release mechanism for the encapsulated FU molecules, contrasting with the uncontrolled release of the drug from FU@ZIF-8 alone. This control was attributed to the surface coating of FU@ZIF-8 particles by LP layers (Scheme 9).

Another study from our laboratory delved into the formation of a nanocomposite hydrogel made up of Pd@ZIF-8 NPs and LP.<sup>87</sup> This composite demonstrated size-selective catalytic hydrogenation of olefins under mild conditions. Pd nanoparticle-decorated ZIF-8 and LP were employed to form a stable hydrogel using a MeOH/water solvent mixture. The PXRD pattern of the composite xerogel revealed the coexistence of both ZIF-8 and LP components within the composite. FESEM images of the Pd@ZIF-8 + LP xerogel unveiled an interwoven network structure, with the Pd@ZIF-8 particles embedded within a layered LP clay matrix. It was envisaged that in the Pd@ZIF-8 + LP xerogel, the inclusion of an extra layer of LP in Pd@ZIF-8 has the potential to create additional

variations in the diffusion of reactant molecules, resulting in a finer sieving effect on reactants. To verify this, we conducted various hydrogenation experiments on a range of alkenes using both Pd@ZIF-8 and Pd@ZIF-8 + LP materials. These reactions were carried out under optimized conditions, allowing for direct comparison. The results revealed that the presence of LP introduced an added sieving effect, leading to lower conversions over Pd@ZIF-8 + LP as compared to Pd@ZIF-8. This effect was particularly notable for alkenes containing cyclic C6 rings. For instance, while both catalysts showed high conversions for simple linear 1-hexene, Pd@ZIF-8 exhibited significantly higher conversion rates than Pd@ZIF-8 + LP. Similarly, conversions were substantially lower for styrene and 1-limonene over Pd@ZIF-8 + LP compared to Pd@ZIF-8. Interestingly, mixtures of alkenes were also tested for hydrogenation, revealing that Pd@ZIF-8 + LP selectively hydrogenated 1-hexene while leaving 1-limonene unaffected. In contrast, Pd@ZIF-8 demonstrated conversions of both substrates. On the other hand, Pd@ZIF-8 + LP exhibited remarkable stability and maintained its activity over four cycles, with negligible changes observed in the conversion of 1-hexene.

Browe *et al.*<sup>88</sup> demonstrated that integrating a high-aspect-ratio and impervious filler like LP with a reactive UiO-66-NH<sub>2</sub> filler component in polyethylene oxide (PEO) preserves the alignment of the high-aspect-ratio component parallel to the film surface. This not only enhanced the barrier protection attributes of the hybrid material, but also enabled high water vapor transport rates (WVTR) (Fig. 5).

The pH sensitivity of the UiO-66-NH<sub>2</sub> structure was investigated, revealing that it only undergoes degradation at high pH levels. PXRD pattern analysis suggested that at pH 8, the struc-



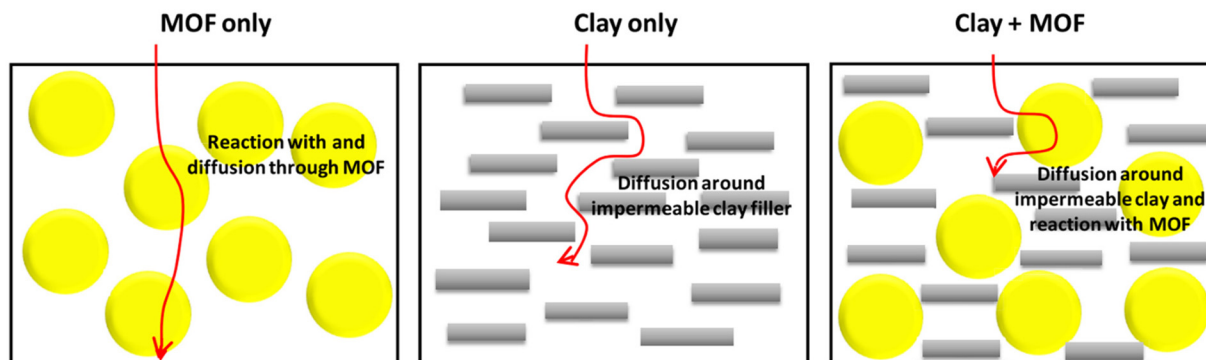


Fig. 5 Toxic gas permeation behaviour for different filler combinations at equal times: (left) polymer + MOF, (middle) polymer + clay, and (right) polymer + MOF + clay. This figure has been adapted from ref. 88 with permission from the American Chemical Society, copyright 2021.

tures of both UiO-66-NH<sub>2</sub> and LP were preserved, while UiO-66-NH<sub>2</sub> lost all of its crystallinity at pH 10. As a result, films were crafted at three different pH levels (pH 8, 9, and 10), incorporating the MOF, named PEO-U-pH *x*, LP, labeled as PEO-LRD-pH *x*, and a combination of both MOF and LP, referred to as PEO-U-LRD-pH *x*. Furthermore, a PEO control film was produced to assess the comparative properties and efficiency of composite films under different conditions. The composite films prepared at pH 8 exhibited large spherulitic structures within the standard PEO film, which displayed a reduction in size on the addition of LP, indicating that the PEO loses its complete crystallinity. SEM images of the PEO-U-LRD composite at pH 8 revealed that the dispersion of UiO-66-NH<sub>2</sub> within the PEO-U-LRD composite appeared relatively uniform, although with larger aggregates compared to the PEO-U counterpart, possibly attributed to interactions with LP platelets. On the other hand, at pH levels of 9 and 10, a less homogeneous distribution was observed, characterized by distinct regions of aggregated UiO-66-NH<sub>2</sub> particles.

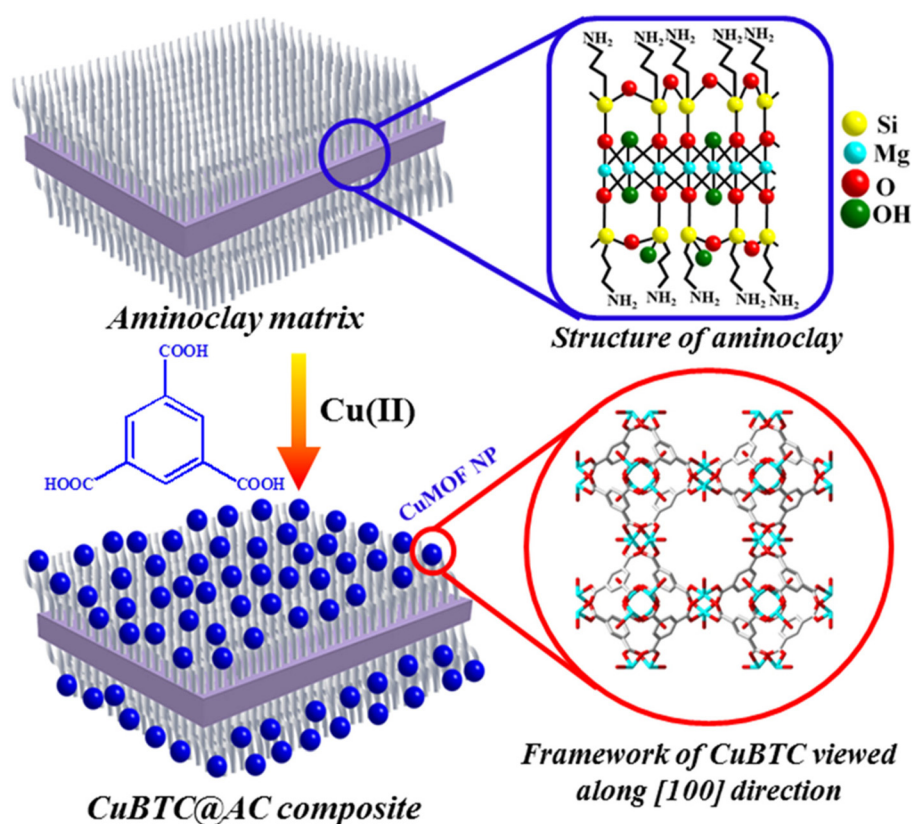
Miao *et al.*<sup>89</sup> investigated the fabrication of Co-based spinel nanocrystals (NCs) through the thermal breakdown of clay structures composed of LP, which were gathered on ZIF-67 frameworks ([Co(mim)<sub>2</sub>]<sub>*n*</sub>, mim = 2-methylimidazolate). This work showcased the fabrication of a Co-based zeolitic imidazolate composite by coating the ZIF-67 framework using LP *via* supersonic mixing, named LP@ZIF-67 with rhombic dodecahedral morphologies. LP@ZIF-67 was used to embed spinal NCs, *i.e.*, Co-Fe-Mg-O, by thermal treatments. During the process, the Mg and Fe isomorphs within LP underwent a transformation into FeCo<sub>2</sub>O<sub>4</sub> and MgCo<sub>2</sub>O<sub>4</sub> NCs at a temperature of approximately 400 °C. Alongside the formation of Co<sub>3</sub>O<sub>4</sub> NPs originating from the breakdown of ZIF-67, spinel structures comprising FeCo<sub>2</sub>O<sub>4</sub> and MgCo<sub>2</sub>O<sub>4</sub> were also identified and embedded within the LP cages. The adsorption-desorption isotherms of the synthesized ZIF-67 exhibited type-I behaviour. The SSA of ZIF-67 was found to be 1521 m<sup>2</sup> g<sup>-1</sup>, while LP@ZIF-67 with LP loading of 8 wt% exhibited a reduced SSA of 826.5 m<sup>2</sup> g<sup>-1</sup>, confirming the integration of LP with ZIF-67. This decrease was attributed to the packing of clay sheets, which reduced the SSA. After calcination, the SSA of

LP@ZIF-67 was found to be 135 m<sup>2</sup> g<sup>-1</sup> with type-IV behaviour. The resulting LP@spinel composites exhibited promising catalytic properties in the molecular oxidation of cyclohexane.

#### 4.4. MOF-aminoclay composites

Magnesium phyllosilicate functionalized with aminopropyl groups, known as AC, is a synthetic, highly water-dispersible clay, which was first reported by Mann and co-workers.<sup>12</sup> AC was synthesized by the co-condensation of magnesium chloride and 3-aminopropyltriethoxysilane (APTES), where the high pH of APTES facilitated catalysis, without requiring an additional catalyst.<sup>12</sup> APTES undergoes hydrolysis in the solution, reacting with magnesium chloride to form AC at room temperature. AC exhibits a greatly disordered talc-like 2:1 trioctahedral smectite structure, including a central brucite sheet with octahedrally coordinated MgO/OH chains, which are surrounded on both sides by an aminopropyl-functionalized silicate network (Scheme 3). Inspired by the fact that AC can act as an excellent structural template to stabilize metal nanoparticles (MNPs), for the first time, our group decided to explore the use of AC in MOF chemistry to furnish small MOF NPs supported on the clay matrix.<sup>90</sup> Our research indicated that the functional amine groups within AC play a dual role as nucleation and anchoring sites for ultra-small NPs of the MOF {[Cu<sub>3</sub>(BTC)<sub>2</sub>(H<sub>2</sub>O)<sub>2</sub>].*x*H<sub>2</sub>O} (CuBTC; BTC = 1,3,5-tricarboxylic acid), typically measuring 2–3 nm in diameter. Notably, this represents the inaugural report of such ultra-small NPs within the realm of MOF chemistry.<sup>90</sup> This work demonstrated that the combination of such ultra-small MOF NPs grown on the amine-functionalized clay could meet the challenge of furnishing a water-dispersible MOF composite, exhibiting enhanced CO<sub>2</sub> adsorption, separation and catalytic conversion (Scheme 10).

Three different composites were synthesized by varying the loading of AC, namely CuBTC@AC-1, CuBTC@AC-2 and CuBTC@AC-3 and the PXRD patterns of these composites suggested the formation of the pure phase of pristine CuBTC within the composites. TEM analysis (Fig. 6) demonstrated the successful stabilization of small MOF NPs on a layered AC template in both the CuBTC@AC-1 and CuBTC@AC-2 composites, while the 3<sup>rd</sup> composite exhibited an irregular morphology,



**Scheme 10** Schematic representation of the synthesis of the CuBTC@AC composite from the CuBTC precursors and AC. Blue spheres: CuBTC NPs. This figure has been adapted from ref. 90 with permission from the Royal Society of Chemistry, copyright 2016.

owing to too much clay content. The NPs of **CuBTC@AC-2** have an average size of 2–3 nm and were uniformly distributed on the AC layers, resulting in a stable dispersion in water, which remained stable for over 6 hours, as compared to that of bulk CuBTC (which is precipitated within 15 minutes).

Notably, **CuBTC@AC-2** exhibited a substantially elevated  $\text{CO}_2$  uptake capacity at 298 K and 1 bar, reaching  $120 \text{ mL g}^{-1}$ , a 46% improvement over CuBTC. At zero loading, pristine CuBTC exhibited an isosteric heat of adsorption ( $Q_{\text{st}}$ ) of  $24 \text{ kJ mol}^{-1}$ , while **CuBTC@AC-2** showed a higher value of  $38 \text{ kJ mol}^{-1}$ , which closely resembles that observed in certain  $\text{NH}_2$ -functionalized MOFs. The enhanced  $\text{CO}_2$  affinity observed in **CuBTC@AC-2** is attributed to the creation of active sites at the interface between the MOF NPs and AC, facilitating the interaction with quadrupolar  $\text{CO}_2$ . A single-component  $\text{CO}_2$ ,  $\text{N}_2$  and  $\text{CH}_4$  adsorption isotherm analysis at 298 K and 1 bar revealed high  $\text{CO}_2$  selectivity of the **CuBTC@AC-2** composite. Breakthrough column experiments using binary  $\text{CO}_2/\text{N}_2$  and  $\text{CO}_2/\text{CH}_4$  mixtures at room temperature showed significantly longer retention times for  $\text{CO}_2$  in **CuBTC@AC-2**, indicating its effectiveness in  $\text{CO}_2$  gas separation from gas mixtures. At room temperature and 1 bar of  $\text{CO}_2$  pressure, **CuBTC@AC-2** also acts as a catalyst in the cycloaddition process between propylene oxide and  $\text{CO}_2$ , yielding propylene carbonate revealing a significant increase in catalytic activity compared to the pristine

CuBTC MOF. This was attributed to the high  $\text{CO}_2$  absorption ability of **CuBTC@AC-2** and the uniformly distributed ultra-small NPs that served as catalytic sites, enabling greater interaction between the substrate and the catalyst.

In the pursuit of developing more MOF-AC composites, understanding their properties and enhancing their scope in diverse applications, our group next explored the synthesis of flexible MOF@AC composites.<sup>91</sup> Following our effort to develop clay composites of flexible MOFs (F-MOFs), which are well known in the MOF literature for their interesting gas adsorption and separation behaviour,<sup>115,116</sup> we pioneered a novel approach for utilizing AC-templated synthesis to create F-MOF nanocrystals.<sup>91</sup> This method allowed for the construction of new composite materials with tunable gas adsorption and separation properties. The synthesis of F-MOF@AC composites was carried out by using two different 2D F-MOFs:  $\{[\text{Cu}(\text{pyrdc})(\text{bpp})](5\text{H}_2\text{O})\}_n$  (**F-MOF1**) (pyrdc = pyridine-2,3-dicarboxylate; bpp = 1,3-bis(4-pyridyl)-propane) and  $\{[\text{Cu}(\text{dhbc})_2(4,4'\text{-bpy})]\cdot\text{H}_2\text{O}\}$  (**F-MOF2**) (Hdhbc = 2,5-dihydroxybenzoic acid, 4,4'-bpy = 4,4'-bipyridine). Both **F-MOF1** and **F-MOF2** undergo modifications to their structures after dehydration, resulting in a constricted structure, whereas addition of guest molecules causes structural expansion (Scheme 11). Different composites of **F-MOF1**, denoted as **F-MOF1@AC-1**, **F-MOF1@AC-2** and **F-MOF1@AC-3**, were synthesized by alter-

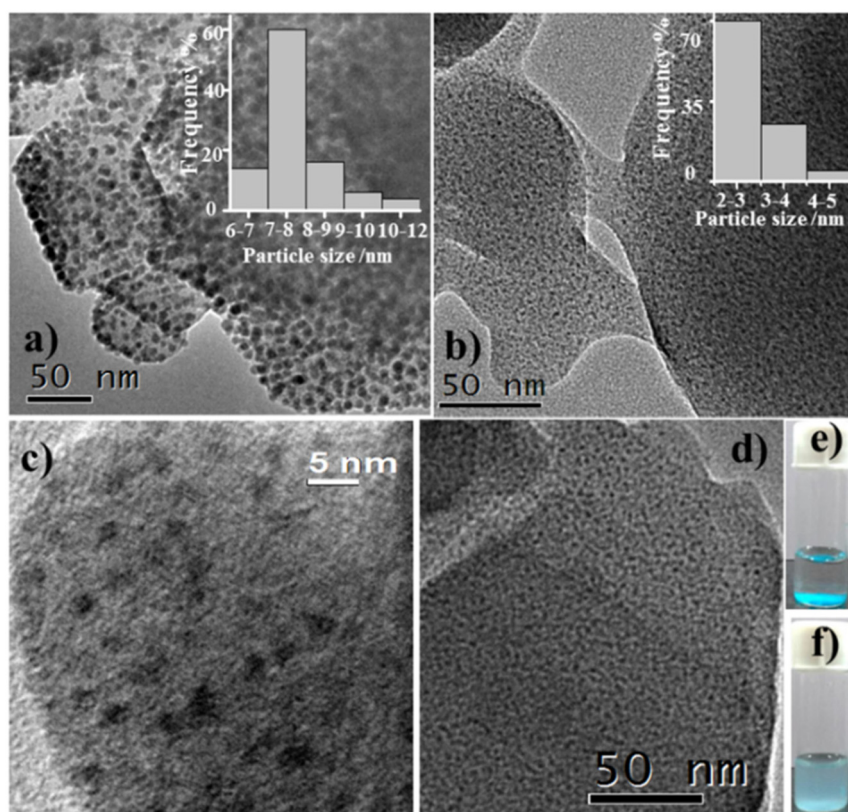
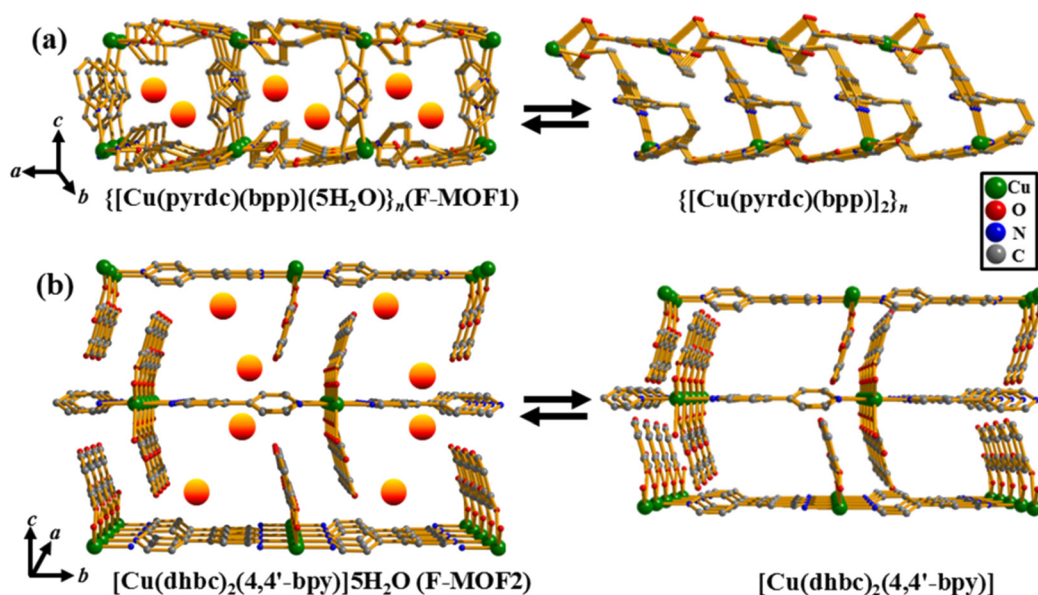


**Fig. 6** TEM images of (a) CuBTC@AC-1, and (b) CuBTC@AC-2 with size distribution histogram plots in the inset. (c) HRTEM image of CuBTC@AC-2 and (d) the sample obtained by the solvothermal reaction of Cu@AC and BTC. Images of dispersion in water of (e) CuBTC 15 minutes and of (f) CuBTC@AC-2 6 hours after preparation. This figure has been adapted from ref. 90 with permission from the Royal Society of Chemistry, copyright 2016.



**Scheme 11** Schematic representation showing the guest-induced structural change in (a) F-MOF1 and (b) F-MOF2. This figure has been adapted from ref. 91 with permission from the Royal Society of Chemistry, copyright 2017.

ing the AC loading. TEM images of all the composites exhibit the growth and stabilization of MOF nanocrystals seamlessly dispersed within the layered AC template, similar to the pre-

viously reported rigid CuBTC MOF grown on AC.<sup>90</sup> With an increase of AC loading in the F-MOF composites, the layers of AC were found to increase in the composites. N<sub>2</sub> sorption iso-



therms at 77 K were recorded with the activated composites, revealing notable type-IV-like behaviour for **F-MOF1@AC-1**, while **F-MOF1@AC-2** and **F-MOF1@AC-3** exhibited negligible adsorption (Fig. 7a). **F-MOF1@AC-1** exhibited enhanced  $N_2$  uptake in comparison with the parent **F-MOF-1**, which was attributed to the presence of finely dispersed MOF NPs, along with enhanced accessibility and porosity relative to the bulk-sized **F-MOF-1**. The presence of micropores and mesopores, owing to the distribution of MOF NPs between AC layers and void formation at the MOF NP-AC interface, further contributed to the elevated uptake.

The  $CO_2$  adsorption behaviour of **F-MOF1@AC-1** and **F-MOF1** at 195 K revealed stepwise  $CO_2$  adsorption by **F-MOF1@AC-1**, while pristine **F-MOF1** showed gated behaviour (Fig. 7b). The initial  $CO_2$  uptake was attributed to the micropores in the **F-MOF1@AC-1** composite and the sharp uptake beyond  $P = 0.39$  bar was assigned to the open phase of **F-MOF1** in the porous composite. The other two composites, **F-MOF1@AC-2** and **F-MOF1@AC-3**, exhibited gated behaviour, and the step/gate pressures of all the composites were found to be higher than the gate-opening pressure of desolvated **F-MOF1**. Such tunable step/gate pressure in the composites was attributed to the fact that the activated phase of **F-MOF1** is more stabilized in the composites, as a number of amine groups of AC are present in the composites, which helps in stabilization of the activated phase of **F-MOF1** via non-covalent interactions. To check whether or not AC can stabilize versatile F-MOF NPs, resulting in novel F-MOF@AC composites, a different F-MOF (**F-MOF2**) was next explored.<sup>91</sup>

Upon dehydration, **F-MOF2** was reported to undergo a transition from porous to non-porous structure due to the gliding action of two  $\pi$ -stacked sheets. Two different **F-MOF2@AC** composites (**F-MOF2@AC-1** and **F-MOF2@AC-2**) with different AC content were developed and thoroughly characterized.

Breakthrough column experiments at 298 K demonstrated the potential of the **F-MOF2@AC-1** composite to separate  $CO_2$  gas from a mixture of  $CO_2/N_2$  and  $CO_2/CH_4$  gases.

After investigating AC as a template to grow both rigid and flexible MOFs, the next effort of our group was to study the self-assembly of MOF NPs with AC. Subsequently, we reported the *in situ* growth of self-assembled AC nanocomposites (Scheme 12)<sup>92</sup> of the prototype zeolitic imidazolate framework, ZIF-8,<sup>117</sup> ( $Zn[MeIm]_2$ ; MeIm = 2-methylimidazolate). Compared to the pure ZIF-8 MOF NPs, the ZIF-8@AC composites showed larger surface area and enhanced  $N_2$  and  $CO_2$  adsorption capacities due to the formation of random voids and active sites at the MOF-clay interface. Four different composites were synthesized by changing the amount of AC loading and denoted as **ZIF-8@AC-1**, **ZIF-8@AC-2**, **ZIF-8@AC-3** and **ZIF-8@AC-4**. The driving force for the formation of these composites is a distinct interaction between unsaturated Zn(II) metal sites present in the ZIF-8 NPs and the amine groups ( $NH_2$ ) present in AC. Such an interaction was also confirmed by the reduction of the positive zeta potential on the surface of ZIF-8, as well as from IR and Raman studies. As the AC layers coated the surface of the ZIF-8 particles, the zeta potential in the composites having higher clay content progressively decreased.

Morphology studies by FESEM and TEM revealed that all the composites have assemblies of ZIF-8 NPs fused with AC (Fig. 8), while the parent ZIF-8 NPs and pristine AC exhibited hexagonal-like shapes and 2D sheet-like structures, respectively. With an increase in AC content, the composites showed a transition from hexagonal-like particles to spherical particles. The composites with higher clay content, such as **ZIF-8@AC-3** and **ZIF-8@AC-4**, revealed visible AC layers that coated ZIF-8 particle surfaces and layered junctions between the ZIF-8 NPs (Fig. 8c). Out of all the composites, **ZIF-8@AC-2** showed the

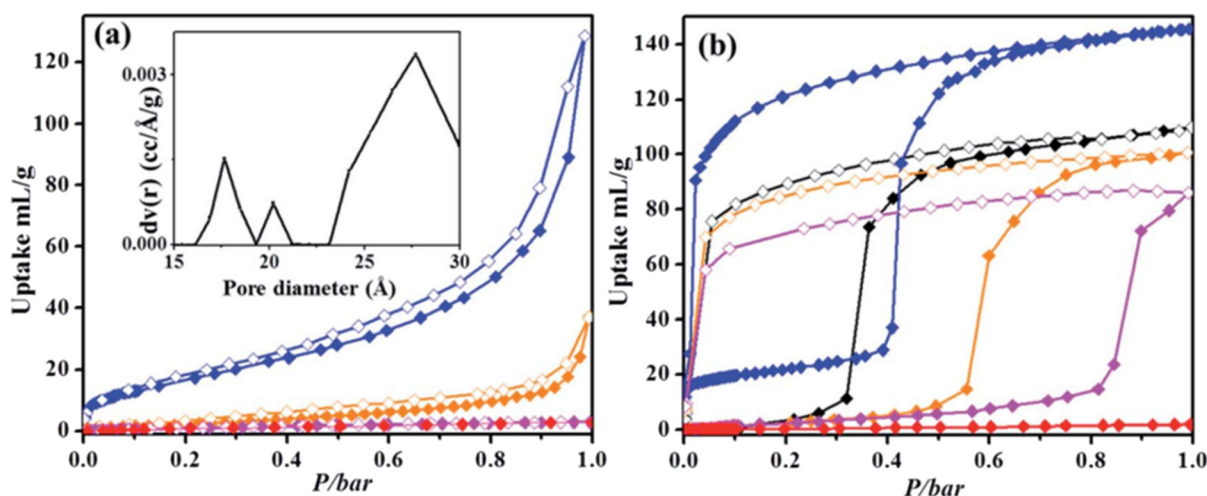
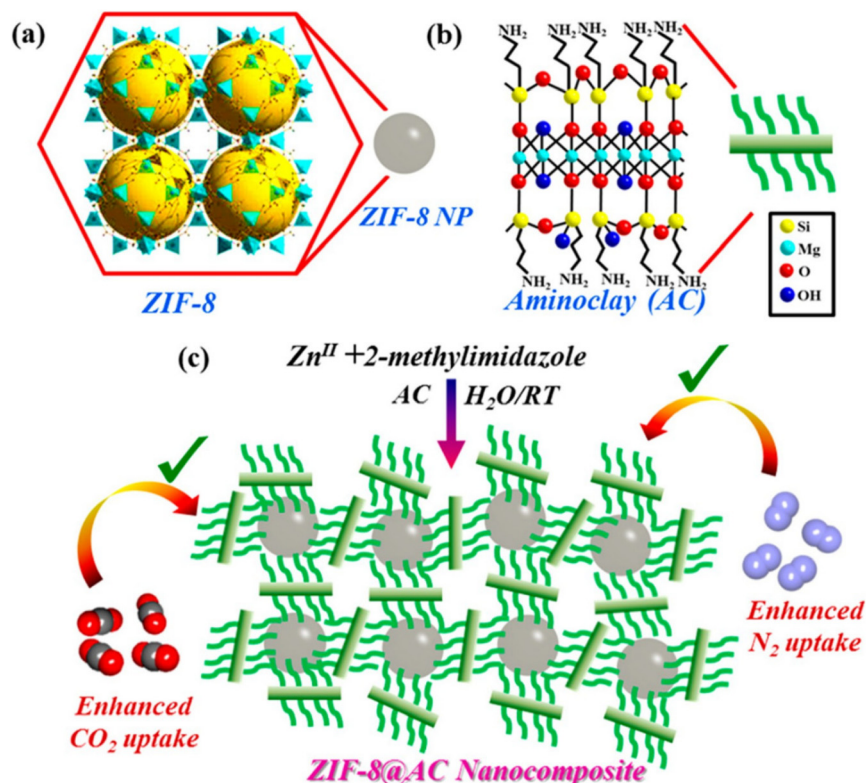


Fig. 7 (a)  $N_2$  adsorption isotherms at 77 K. The pore size distribution of **F-MOF1@AC-1** is shown in the inset. (b)  $CO_2$  adsorption isotherms at 195 K. Color code: **F-MOF1**: black, AC: red, **F-MOF1@AC-1**: blue, **F-MOF1@AC-2**: orange, and **F-MOF1@AC-3**: magenta (open and closed symbols denote adsorption and desorption, respectively). The isotherms for composites represent  $N_2$  uptake per gram of the respective composite. This figure has been adapted from ref. 91 with permission from the Royal Society of Chemistry, copyright 2017.





**Scheme 12** (a) Structural representation of ZIF-8, (b) structure and schematic diagram of AC and (c) schematic representation of the synthesis and self-assembly of ZIF-8 and AC toward the formation of nanocomposites. Colour code: ZIF-8 NPs, gray. This figure has been adapted from ref. 92 with permission from the American Chemical Society, copyright 2017.

best performance, exhibiting a 42% increase in the BET surface area, while the CO<sub>2</sub> uptake at 298 K was doubled relative to the pristine ZIF-8 NPs. *In situ* Raman studies for this composite under a CO<sub>2</sub> atmosphere indicated that the amine groups in the composite act as CO<sub>2</sub> binding sites, facilitating CO<sub>2</sub> adsorption.

By developing binary and ternary MOF-clay nanocomposites adopting an *in situ* hydrothermal process, our group recently presented a new approach for atmospheric water harvesting (AWH) suitable for indoor environments (Scheme 13).<sup>93</sup> A series of CuBTC/AC/GO MOF-clay nanocomposites (Cu<sub>3</sub>(BTC)<sub>2</sub>(H<sub>2</sub>O)<sub>3</sub>; BTC = benzene-1,3,5-tricarboxylate and GO = graphene oxide) were synthesized by adding different amounts of AC and GO to the pristine CuBTC MOF. Three different binary composites were synthesized, denoted as CuBTC/AC-1, CuBTC/AC-2 and CuBTC/AC-3, by adding different proportions of AC (6.2, 8.9 and 14.1%, respectively). The ternary composites, named CuBTC/AC/GO-1, CuBTC/AC/GO-2 and CuBTC/AC/GO-3, were also synthesized by adding 9 wt% of GO to the CuBTC/AC composites. All the composites showed larger specific surface areas in comparison with that of the pristine CuBTC MOF. The composite CuBTC/AC/GO-2 exhibited a significant increase in the specific surface area (1569 m<sup>2</sup> g<sup>-1</sup>) relative to that of the pristine CuBTC MOF (1260 m<sup>2</sup> g<sup>-1</sup>), which may be associated with the decreased diffusion barrier due to the successful formation of

MOF NPs and the development of interfacial voids within the composites, resulting in an increased number of accessible adsorption sites for N<sub>2</sub>. Furthermore, the dynamic dispersion ability of AC in water provides enhanced water stability to the composite. Subsequently, the addition of GO, having prolonged heat conduction capability, aids in the easy release of water during desorption.

The ternary composites demonstrated notably improved water adsorption performance, achieving an enhanced water uptake of 716 cm<sup>3</sup> g<sup>-1</sup> under arid-humid-fog conditions. This effectively overcomes the shortcomings observed in the individual performances of both the MOF and the combined GO and AC components. A prototype device was designed with three compartments for water generation, featuring a temperature-controlled system for efficient water vapor condensation. The ternary MOF nanocomposite (CuBTC/AC/GO) exhibited better efficiency for indoor atmospheric water harvesting. The composite underwent testing under a relative humidity (RH) range of 85%–90% at temperatures of 65, 75, 85, and 90 °C. It was observed that as the temperature increased, there was a sharp increase in water uptake, reaching a maximum of 0.67 g g<sup>-1</sup> at 90% RH, which is a 39.5% increase compared to that of bulk CuBTC. Furthermore, variations in RH levels from 10%, 30%, 50%, 70%, to 90% at a constant temperature of 20–25 °C were examined to assess water harvesting performance, resulting in a maximum amount of water collection of 0.43 g g<sup>-1</sup>.

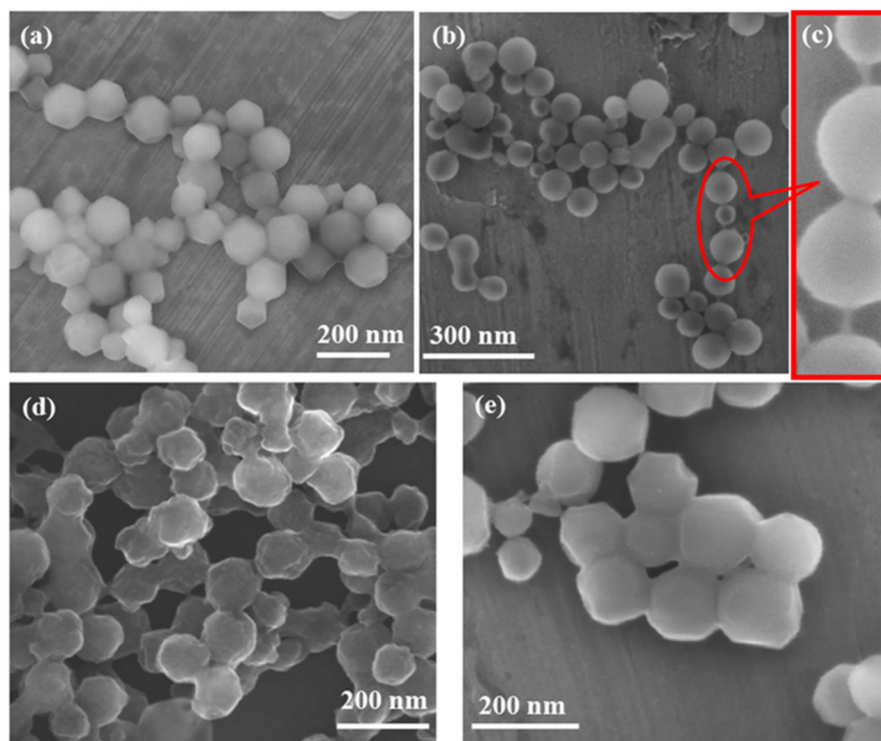
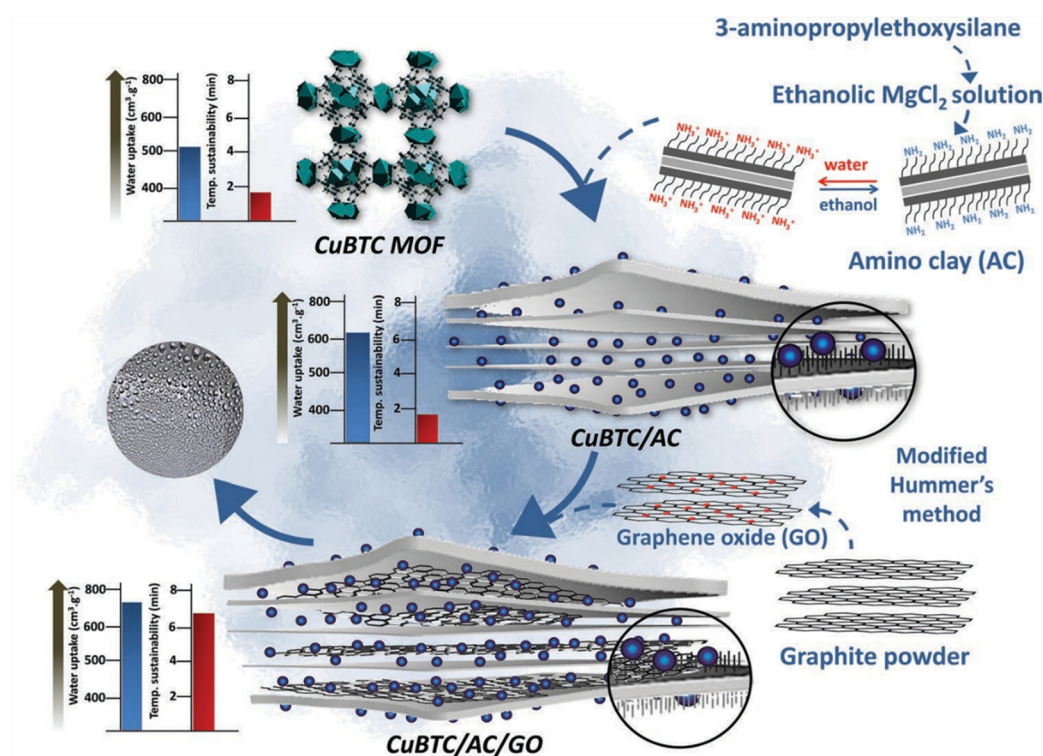


**Fig. 8** FESEM images of (a) ZIF-8@AC-1, (b) ZIF-8@AC-2, (d) ZIF-8@AC-3, and (e) ZIF-8@AC-4. (c) Enlarged view of a portion of ZIF-8@AC-2 in (b) showing that the NPs are connected through the thin junctions of AC. This figure has been adapted from ref. 92 with permission from the American Chemical Society, copyright 2017.



**Scheme 13** Schematic diagram showing MOF NPs stabilized on an AC and AC/GO mixed-matrix template. This figure has been adapted from ref. 93 with permission from John Wiley & Sons – Books, copyright 2022.

The prototype nanocomposite (CuBTC/AC/GO) showed an overall water harvesting efficiency of 63.4%–68.5%. An autonomous indoor water harvesting method was also established, which allowed for a continuous cycle of capture and release, yielding an improved water collection rate of  $0.445 \text{ g g}^{-1} \text{ day}^{-1}$ .

In a recent study, we synthesized AC nanocomposites of the MIL-101(Cr) framework (MIL = Materials of Institute Lavoisier), which served as an excellent heterogeneous catalyst for the conversion of the greenhouse gas  $\text{CO}_2$  into cyclic carbonates.<sup>94</sup> Interestingly, these composites exhibited good catalytic efficacy, and showcased complete conversion under ambient conditions, while most of the MIL-101-based materials typically require either high temperature and pressure or a longer reaction time, or a combination of all the parameters. We synthesized three different composites by adding different amounts of AC, denoted as **MIL-101(Cr)/AC-1**, **MIL-101(Cr)/AC-2** and **MIL-101(Cr)/AC-3** and the PXRD patterns of the composites suggested the formation of the pure phase of MIL-101(Cr) (PMIL) within the composites. The FESEM images of all the composites showed the formation of a self-assembled network structure for all the composites. **MIL-101(Cr)/AC-1** and **MIL-101(Cr)/AC-2** revealed particle size distributions in the range of 70–90 nm and 50–70 nm, respectively. For the **MIL-101(Cr)/AC-2** composite, the particle distribution is more homogeneous as compared to the other composites, and this results in the enhanced solution processability of this composite (its dispersion is stable for more than 4 days in methanol). This composite also showed the best catalytic activity for the  $\text{CO}_2$  cycloaddition reaction and exhibited 99.9% conversion in cycloaddition reactions with various epoxide substrates (Table 1) under ambient reaction conditions (at 1 bar  $\text{CO}_2$  pressure and temperature of 30/40 °C). **MIL-101(Cr)/AC-2** also exhibited excellent heterogeneity and recyclability, maintaining its efficiency over multiple cycles (up to 5 cycles) without any significant loss in catalytic activity.

Mohammadi *et al.*<sup>95</sup> synthesized a porous aluminium-based MOF–AC nanocomposite denoted as MIL-53(Al)@AC using an environmentally friendly hydrothermal method. FESEM images revealed that the MIL-53(Al)@AC composite possessed characteristics of both MIL-53(Al), with its rod-like structure, and AC, particularly evident at the junctions among the MIL-53(Al) MOF particles. Type-IV behaviour was observed for all the samples when the  $\text{N}_2$  adsorption–desorption isotherms were measured. The composite showed a larger specific surface area ( $1536.73 \text{ m}^2 \text{ g}^{-1}$ ) in comparison with that of the pristine MIL-53(Al) MOF ( $1294.34 \text{ m}^2 \text{ g}^{-1}$ ). The enhancement of the surface area was attributed to the interaction between AC and MIL-53(Al), which effectively mitigated crystal aggregation, improving the accessibility of MIL-53(Al) to  $\text{N}_2$  molecules. Additionally, the formation of voids at the interface of MIL-53(Al)@AC layers further contributed to the increased surface area of the nanocomposite. The authors also explored the sorption capacity of the nanocomposite under different conditions, such as pH, temperature, and ionic strength, and found that the MIL-53(Al)@AC composite had a higher sorption capacity compared to that of pristine MIL-53(Al). The

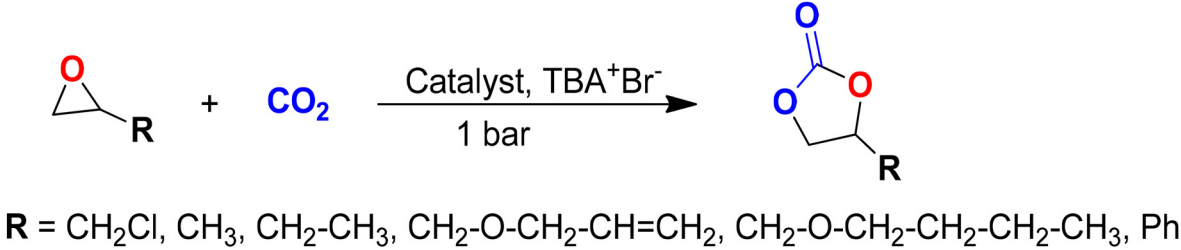
composite demonstrated exceptional sorption capacities for cephalosporin antibiotics cefixime (CFX) and cephalixin (CPX).

In a recent study, Cao *et al.*<sup>96</sup> developed innovative composite NPs denoted as  $\text{Fe}_3\text{O}_4\text{@AC-NH}_2\text{@Cu-opa}$  ( $\text{AC-NH}_2 = \text{AC}$ ,  $\text{Cu-opa} = [\text{Cu}(\text{opa})(\text{bipy})_{0.5}(\text{H}_2\text{O})]_n$  ( $\text{H}_2\text{opa} = 3\text{-(4-oxypyridinium-1-yl) phthalic acid}$ )). These NPs played a dual role as both adsorbents and catalysts for the removal of phenolic compounds from wastewater. The typical synthesis of the core-shell-structured  $\text{Fe}_3\text{O}_4\text{@AC-NH}_2\text{@Cu-MOF}$  NPs is presented in Scheme 14. Initially, a layer of AC was deposited onto the pre-synthesized magnetic  $\text{Fe}_3\text{O}_4$  NPs by an *in situ* synthesis approach, resulting in the formation of  $\text{Fe}_3\text{O}_4\text{@AC-NH}_2$ . To initiate the growth of a thin Cu-MOF shell onto the AC layer,  $\text{Fe}_3\text{O}_4\text{@AC-NH}_2$  was dispersed in a mixture of water/ethanol and then the precursor solution of Cu-opa was added under solvothermal conditions, leading to the formation of the final compound, named  $\text{Fe}_3\text{O}_4\text{@AC-NH}_2\text{@Cu-opa}$  NPs. The amine ( $\text{NH}_2$ ) groups present in AC act as binding sites for metals, enabling the growth of small MOF NPs. The surface morphology and structural features of  $\text{Fe}_3\text{O}_4$ ,  $\text{Fe}_3\text{O}_4\text{@AC-NH}_2$ , and  $\text{Fe}_3\text{O}_4\text{@AC-NH}_2\text{@Cu-opa}$ , as observed by SEM analysis, demonstrated that the  $\text{Fe}_3\text{O}_4$  NPs displayed a uniform diameter of approximately 300 nm with a rough, spherical surface and coating  $\text{Fe}_3\text{O}_4$  with AC resulted in globular structures of around 310 nm size, indicating a 5 nm thickness of the AC shell. Further coating with Cu-MOF revealed a layered Cu-opa shell of approximately 10 nm thickness, confirming the successful synthesis of core-shell structured  $\text{Fe}_3\text{O}_4\text{@AC-NH}_2\text{@Cu-opa}$  microspheres. SEM elemental mapping confirmed the uniform distribution of Mg, Cu, and Fe elements, validating the effectiveness of this synthetic approach.

$\text{N}_2$  adsorption–desorption isotherms were measured to evaluate the specific surface areas of  $\text{Fe}_3\text{O}_4$ ,  $\text{Fe}_3\text{O}_4\text{@AC-NH}_2$ , and  $\text{Fe}_3\text{O}_4\text{@AC-NH}_2\text{@Cu-opa}$ . The  $\text{Fe}_3\text{O}_4$  NPs displayed a type-IV isotherm with hysteresis occurring at  $P/P_0 = 0.7\text{--}1.0$ , which is typical of mesoporous materials. The BET surface area of  $\text{Fe}_3\text{O}_4$  was found to be  $68.6 \text{ m}^2 \text{ g}^{-1}$ . Upon clay coating,  $\text{Fe}_3\text{O}_4\text{@AC-NH}_2$  NPs displayed a similar isotherm and hysteresis to those of  $\text{Fe}_3\text{O}_4$ , with a decrease in the specific surface area of  $\text{Fe}_3\text{O}_4\text{@AC-NH}_2$  ( $53.4 \text{ m}^2 \text{ g}^{-1}$ ). Subsequently,  $\text{Fe}_3\text{O}_4\text{@AC-NH}_2\text{@Cu-opa}$  exhibited a type-I isotherm after Cu-MOF coating that indicated the formation of micropores on the outer layer. The specific surface area of  $\text{Fe}_3\text{O}_4\text{@AC-NH}_2\text{@Cu-opa}$  was approximately  $719.1 \text{ m}^2 \text{ g}^{-1}$ , suggesting a significant increase in the SSA facilitated by Cu-opa. The authors also explored the interaction of  $\text{Fe}_3\text{O}_4\text{@AC-NH}_2\text{@Cu-opa}$  NPs with phenol molecules. By incorporating Cu-opa, which boasted substantial electron-deficient channels, the NPs exhibit enhanced adsorption capabilities. This enhancement is reflected in the rapid uptake of phenol, with equilibrium reached within 120 minutes and a notable adsorption capacity of  $107.42 \text{ mg g}^{-1}$ . Kinetic modeling underscored the chemical nature of the adsorption process, favoring a pseudo-second-order mechanism over a pseudo-first-order one. Further analysis using Langmuir and Freundlich iso-



**Table 1** CO<sub>2</sub> cycloaddition to different epoxides using MIL-101(Cr)/AC-2 as a heterogeneous catalyst<sup>a</sup>

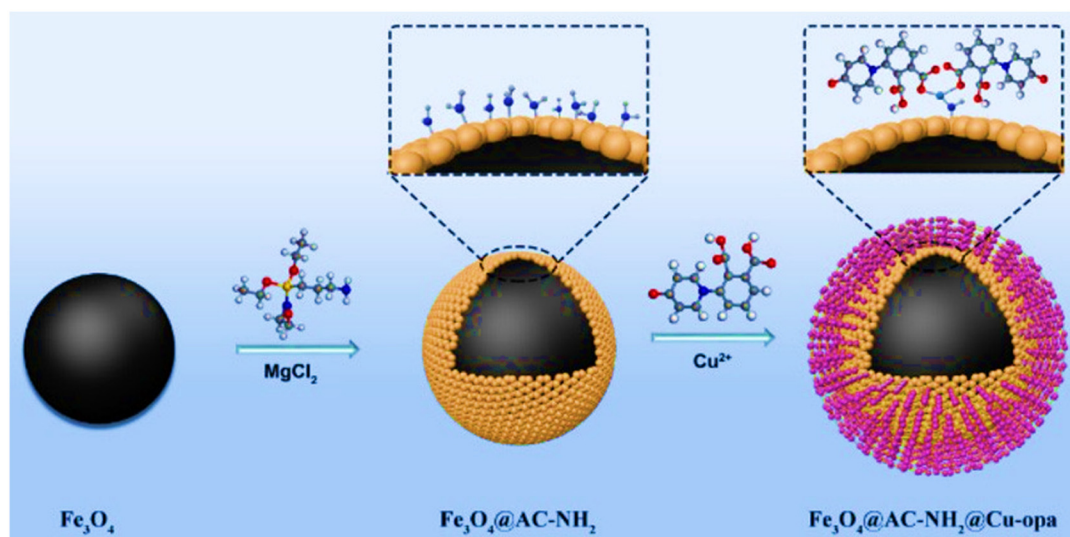
|  |            |          |                  |          |                |
|--|------------|----------|------------------|----------|----------------|
| Entry  | Substrates | Products | Temperature (°C) | Time (h) | Conversion (%) |
| 1  |            |          | 30               | 6        | 99.9           |
| 2  |            |          | 30               | 6        | 99.9           |
| 3  |            |          | 40               | 6        | 99.9           |
| 4  |            |          | 40               | 12       | 99.9           |
| 5  |            |          | 40               | 15       | 99.9           |
| 6  |            |          | 40               | 48       | 99.9           |

<sup>a</sup> Reaction conditions: 9.2 mmol respective epoxide, 30 mg of activated catalyst and 0.92 mmol TBA<sup>+</sup>Br<sup>-</sup> under optimized reaction conditions, *i.e.*, 1.0 bar CO<sub>2</sub> and at optimized temperature (30/40 °C). Conversion (%) was calculated from the <sup>1</sup>H NMR spectra. This table has been adapted from ref. 94 with permission from the Royal Society of Chemistry, copyright 2024.

therms revealed a compelling fit of both models to the experimental data. The Langmuir model revealed a notable monolayer adsorption capacity of 166.39 mg g<sup>-1</sup>. This implied that the surface of the NPs provided highly effective sites for phenol adsorption. The robust adsorption was further supported by the substantial Langmuir adsorption equilibrium constant (*k<sub>L</sub>*) of 7.16 L mg<sup>-1</sup>, indicating strong binding between the NPs and the phenol molecules. The catalytic properties of Fe<sub>3</sub>O<sub>4</sub>@AC-NH<sub>2</sub>@Cu-opa in phenol degradation were also investigated under Fenton-like conditions using H<sub>2</sub>O<sub>2</sub>. The results showed complete disappearance of phenol within 15 minutes in Fe<sub>3</sub>O<sub>4</sub>@AC-NH<sub>2</sub>@Cu-opa/H<sub>2</sub>O<sub>2</sub>, whereas Fe<sub>3</sub>O<sub>4</sub>/H<sub>2</sub>O<sub>2</sub> took 60 minutes. However, only 60% of phenol was removed in 60 minutes using Fe<sub>3</sub>O<sub>4</sub>@AC-NH<sub>2</sub>@Cu-opa. The

heterogeneous Fenton-like reactions were catalyzed using Fe<sub>3</sub>O<sub>4</sub> or Fe<sub>3</sub>O<sub>4</sub>@AC-NH<sub>2</sub>@Cu-opa NPs, leading to rapid phenol degradation, which was attributed to the activation of H<sub>2</sub>O<sub>2</sub> dissociation by Fe<sub>3</sub>O<sub>4</sub>. The degradation mechanism involved breaking the benzene ring and oxidizing the organic chain compound facilitated by hydroxyl radicals (·OH) produced *via* the Fe<sup>2+</sup> from Fe<sup>3+</sup> redox process. The Fe<sub>3</sub>O<sub>4</sub>@AC-NH<sub>2</sub>@Cu-opa NPs exhibited a higher pseudo-first-order rate constant compared to that of Fe<sub>3</sub>O<sub>4</sub>, indicating superior efficiency in phenol degradation, which was attributed to a synergistic effect between adsorption and oxidation, enhancing phenol removal, with the strong adsorption capacity of Fe<sub>3</sub>O<sub>4</sub>@AC-NH<sub>2</sub>@Cu-opa's playing a key role. The nanoparticle's ability to degrade phenol over multiple cycles





**Scheme 14** Schematic representation of the synthetic procedure of the core-shell-structured  $\text{Fe}_3\text{O}_4@AC\text{-NH}_2@Cu\text{-opa}$  NPs. This figure has been adapted from ref. 96 with permission from the Royal Society of Chemistry, copyright 2024.

and its effectiveness in real wastewater samples highlighted its promising role in wastewater treatment.

Recently, Lee *et al.*<sup>97</sup> synthesized an Ag-MgAC-MIL-53(Fe)-based MOF composite electrode sensor. MIL-53(Fe) has active metal sites, while 2D AC has a number of amine-functionalized groups, which play important roles as supporting stabilizers and also as efficient linkers between the AgNPs and MIL-53(Fe). However, the AgNPs exhibited attractive chemical and physical properties that were stabilized and homogeneously distributed on the MIL-53(Fe) MOF framework due to the presence of AC. The modified electrode demonstrated impressive recyclability, selectivity and stability, showcasing its considerable promise for use in electrochemical sensors for monitoring chloromycetin.

## 5. Summary, challenges and future outlook

In this comprehensive article, we have summarized emerging MOF-clay composites and discussed some representative literature reports, which indicate the promise of these composites as next-generation MOF-based materials with multifaceted functionalities and a broad spectrum of applications. MOFs have been blended with both natural and synthetic clays, and we have summarized both cases, which elucidate the design principles of the desired composites. The selected examples of MOF-clay composites illustrate how a synergistic interplay between both parent materials has mitigated the traditional shortcomings of MOFs, including poor thermal and chemical stability, moisture sensitivity, and solution processability. At the same time, these composites have also shown enhanced properties compared to those of the parent materials or introduced new properties, including gas storage

and separation, pollutant removal, catalysis (organic transformation reactions and photocatalysis), drug delivery, dye removal and degradation, chemical warfare agent simulants,  $\text{CO}_2$  conversion, *etc.*

The field of the emergent MOF-clay composites has great potential, but there are certain drawbacks and challenges too. While certain synthetic routes (discussed in section 3) have been reported for the facile synthesis of composites, the detailed mechanisms of the formation of such composites are not well understood and yet to be explored. The lack of clarity surrounding the synthesis mechanisms of MOF composites could be caused by a number of issues. First, the self-assembly interactions between the MOF precursors/pre-formed MOF particles and clay are complex, sophisticated and often unpredictable. Additionally, different synthetic conditions such as temperature, pH, choice of solvents, *etc.* affect the interactions between the parent materials, adding complexity.

A good number of techniques used to characterize MOF-clay composites have been widely reported, such as PXRD to study their crystalline nature, FTIR and Raman spectroscopy for verification of functional groups and interfacial interactions between the MOF and clay; SEM and TEM for their particle size and morphology;  $\text{N}_2$  adsorption studies and BET analysis to obtain the specific surface area and pore volume; ICP-AES to detect the chemical elements present in the composites; XPS and TGA for studying thermal stability, *etc.*<sup>118</sup> It may be noted that a combination of several techniques are required to adequately characterize MOF-clay composites. The difficulty in the characterization of MOF-clay composites is rooted in the complex and heterogeneous nature of the materials comprising the composites. Furthermore, most of the literature has reported characterization methods that involve post-synthetic examination of the samples and thus the studies may overlook or fail to capture subtle, transient interactions in the

composites. Advanced *in situ* characterization methods could be employed in future, which may shed light on the synthesis in real time and mechanism of the formation of such composites.

While the above aspects pose challenges related to the synthesis and characterization and need to be addressed in the future, the versatile properties and applications of MOF–clay composites are already well documented. To obtain the desired functional composite, the choice of clay is crucial. MOFs can be blended with both natural and synthetic clays (see section 4) and clay minerals have acted as a functional matrix assisting the growth of MOF particles. Additionally, some clay minerals can undergo self-assembly with MOF particles. For instance, AC has been shown to act as a 2D functional scaffold to grow MOF particles<sup>90</sup> and can also undergo self-assembly with MOF nanoparticles.<sup>92</sup>

Synthetic clays seem to be more promising than natural clays to synthesize targeted composites, as they are often suitably functionalized. We believe that water-dispersible synthetic clays, such as AC and LP, hold great promise to furnish water-dispersible MOF composites with enhanced properties, as already shown in the literature.<sup>86–97</sup> The water dispersibility of composites could overcome the limitation of the poor processability of MOFs, ease the fabrication of MOF-based devices and also enhance the scope of MOFs in biomedicine and certain catalytic reactions, where good water dispersion is essential. This could transform MOF chemistry from the laboratory to real-life applications.

MOF–clay composites are an emerging field with great promise to target diverse properties and there are several opportunities to perform detailed studies in the future. The catalytic properties of MOF–AC composites can particularly be studied, as we have recently demonstrated that they can serve as water-dispersible, processable and recyclable catalysts showing enhanced catalytic efficacy for CO<sub>2</sub> conversion reactions compared to the parent MOFs, and require only mild conditions to function.<sup>94</sup> A similar principle can be extended further to generate new nanocomposites targeting various catalytic reactions. Additionally, it is also possible to develop excellent composite catalysts for aqueous and biphasic catalysis, taking the unique advantage of AC.<sup>17,18</sup> We also believe that MOF–LP composites hold great promise to furnish MOF-based hydrogels, which will be easy to synthesize, retain the advantages of hydrogels and can potentially serve as excellent materials for controlled drug delivery, catalysis, and selective guest molecule capture and separation. These hydrogel MOF composites can also be employed as stationary gel matrices suitable for the separation of guest molecules and provide targeted gel chromatographic separation. Enhancing the mechanical properties and obtaining controlled energy transfer are also ideally possible in MOF–clay composites but are yet to be explored. As silicate-based clay minerals typically have a highly stable framework structure and some of the clay-based materials have already shown high mechanical strength,<sup>111</sup> MOF composites with enhanced mechanical properties can be targeted in the future. On the other hand, some specific clays,

such as AC, have shown their ability to provide an ordered arrangement of chromophores, facilitating proficient energy transfer,<sup>14</sup> and the same concept can be extended to develop MOF–AC composites having MOF-based chromophores, targeting efficient light harvesting processes.

The above discussion makes it clear that MOF–clay composites offer unique opportunities to target versatile properties, some of which have already been reported in the literature and more are to be explored. Continued research and development in this field are expected to unlock new functionalities and applications, innovation, and address critical technological and environmental challenges to furnish next-generation materials.

## Data availability

No primary research results, software or code have been included and no new data were generated or analysed as part of this review.

## Conflicts of interest

There are no conflicts to declare.

## Acknowledgements

A. C. sincerely acknowledges the Department of Science and Technology (DST), New Delhi, India for an INSPIRE Faculty Fellowship (DST/INSPIRE/04/2020/001603). Jyoti acknowledges UGC, New Delhi for a Junior Research Fellowship (NTA Ref. No.: 221610140712). T. K. M. acknowledges the Department of Science and Technology (Projects SPR/2021/000592), RAK-CAM (from UAE), SSL, ICMS, and JNCASR for financial support. The SAMat research facility, Sheikh Saqr Senior Fellowship (T. K. M.), is also gratefully acknowledged.

## References

- 1 'Clay Mineral', Encyclopædia Britannica Online. Retrieved from <https://www.britannica.com/science/clay-mineral>, 2016.
- 2 S. M. Auerbach, K. A. Carrado and P. K. Dutta, *Handbook of layered materials*, M. Dekker, 2004.
- 3 F. Bergaya and G. Lagaly, *Dev. Clay Sci.*, 2013, 5, 1.
- 4 A. Kausar, M. Iqbal, A. Javed, K. Aftab, Z.-H. Nazli, H. N. Bhatti and S. Nouren, *J. Mol. Liq.*, 2018, 256, 395.
- 5 H. Tyan, C. Wu and K. Wei, *J. Appl. Polym. Sci.*, 2001, 81, 1742.
- 6 S. Sadjadi, *Appl. Clay Sci.*, 2020, 189, 105537.
- 7 M. Massaro, C. G. Colletti, G. Lazzara, S. Milioto, R. Noto and S. Riela, *J. Mater. Chem. A*, 2017, 5, 13276.
- 8 C. Chuaicham, J. Trakulmututa, K. Shu, S. Shenoy, A. Sriksaow, L. Zhang, S. Mohan, K. Sekar and K. Sasaki, *Separations*, 2023, 10, 77.

- 9 C. Nomicisio, M. Ruggeri, E. Bianchi, B. Vigani, C. Valentino, C. Aguzzi, C. Viseras, S. Rossi and G. Sandri, *Pharmaceutics*, 2023, **15**, 1368.
- 10 H. Tomás, C. S. Alves and J. Rodrigues, *Nanomedicine*, 2018, **14**, 2407.
- 11 S. S. Das, Neelam, K. Hussain, S. Singh, A. Hussain, A. Faruk and M. Tebyetekerwa, *Curr. Pharm. Des.*, 2019, **25**, 424.
- 12 A. J. Patil, E. Muthusamy and S. Mann, *J. Mater. Chem.*, 2005, **15**, 3838.
- 13 V. K. H. Bui, D. Park and Y.-C. Lee, *Chem. Eng. J.*, 2018, **336**, 757.
- 14 K. K. R. Datta, A. Achari and M. Eswaramoorthy, *J. Mater. Chem. A*, 2013, **1**, 6707.
- 15 K. K. R. Datta, M. Eswaramoorthy and C. N. R. Rao, *J. Mater. Chem.*, 2007, **17**, 613.
- 16 K. K. R. Datta, C. Kulkarni and M. Eswaramoorthy, *Chem. Commun.*, 2010, **46**, 616.
- 17 A. S. Kumar, K. K. R. Datta, T. S. Rao, K. V. Raghavan, M. Eswaramoorthy and B. V. S. Reddy, *J. Nanosci. Nanotechnol.*, 2013, **13**, 3136.
- 18 A. S. Kumar, K. K. R. Datta, T. S. Rao, K. V. Raghavan, M. Eswaramoorthy and B. V. S. Reddy, *J. Nanosci. Nanotechnol.*, 2012, **12**, 2000.
- 19 A. A. J. Ranchani, V. Parthasarathy, C. Hu, Y.-F. Lin, K.-L. Tung and R. Anbarasan, *Chem. Eng. Commun.*, 2020, **207**, 871.
- 20 M. Zubair, M. Daud, G. McKay, F. Shehzad and M. A. Al-Harhi, *Appl. Clay Sci.*, 2017, **143**, 279.
- 21 U. Šebenik, R. Lapasin and M. Krajnc, *Carbohydr. Polym.*, 2020, **240**, 116330.
- 22 V. K. A. Shirin, R. Sankar, A. P. Johnson, H. V. Gangadharappa and K. Pramod, *J. Controlled Release*, 2021, **330**, 398.
- 23 M. M. Lezhnina, T. Grewe, H. Stoehr and U. Kynast, *Angew. Chem., Int. Ed.*, 2012, **51**, 10652.
- 24 J. R. Long and O. M. Yaghi, *Chem. Soc. Rev.*, 2009, **38**, 1213.
- 25 H.-C. Zhou, J. R. Long and O. M. Yaghi, *Chem. Rev.*, 2012, **112**, 673.
- 26 H.-C. J. Zhou and S. Kitagawa, *Chem. Soc. Rev.*, 2014, **43**, 5415.
- 27 T. Islamoglu, Z. Chen, M. C. Wasson, C. T. Buru, K. O. Kirlikovali, U. Afrin, M. R. Mian and O. K. Farha, *Chem. Rev.*, 2020, **120**, 8130.
- 28 J. E. Mondloch, R. C. Klet, A. J. Howarth, J. T. Hupp and O. K. Farha, *Handbook of Solid State Chemistry*, Wiley, 2017.
- 29 S. Roy, A. Chakraborty and T. K. Maji, *Coord. Chem. Rev.*, 2014, **273–274**, 139.
- 30 A. Yadav and P. Kanoo, *Chem. – Asian J.*, 2019, **14**, 3531.
- 31 L. E. Kreno, K. Leong, O. K. Farha, M. Allendorf, R. P. Van Duyne and J. T. Hupp, *Chem. Rev.*, 2012, **112**, 1105.
- 32 Z. Hu, B. J. Deibert and J. Li, *Chem. Soc. Rev.*, 2014, **43**, 5815.
- 33 J.-R. Li, J. Sculley and H.-C. Zhou, *Chem. Rev.*, 2012, **112**, 869.
- 34 X. Zhao, X. Bu, T. Wu, S.-T. Zheng, L. Wang and P. Feng, *Nat. Commun.*, 2013, **4**, 2344.
- 35 P. Yadav, P. Bhardwaj, M. Maruthi, A. Chakraborty and P. Kanoo, *Dalton Trans.*, 2023, **52**, 11725.
- 36 P. Yadav, S. Kumari, A. Yadav, P. Bhardwaj, M. Maruthi, A. Chakraborty and P. Kanoo, *ACS Omega*, 2023, **8**, 28367.
- 37 J. A. Mason, M. Veenstra and J. R. Long, *Chem. Sci.*, 2014, **5**, 32.
- 38 Y. Peng, V. Krungleviciute, I. Eryazici, J. T. Hupp, O. K. Farha and T. Yildirim, *J. Am. Chem. Soc.*, 2013, **135**, 11887.
- 39 D. M. D'Alessandro, B. Smit and J. R. Long, *Angew. Chem., Int. Ed.*, 2010, **49**, 6058.
- 40 J. B. DeCoste and G. W. Peterson, *Chem. Rev.*, 2014, **114**, 5695.
- 41 J. Lee, O. K. Farha, J. Roberts, K. A. Scheidt, S. T. Nguyen and J. T. Hupp, *Chem. Soc. Rev.*, 2009, **38**, 1450.
- 42 A. Chakraborty, S. Bhattacharyya, A. Hazra, A. C. Ghosh and T. K. Maji, *Chem. Commun.*, 2016, **52**, 2831.
- 43 A. Yadav, S. Kumari, P. Yadav, A. Hazra, A. Chakraborty and P. Kanoo, *Dalton Trans.*, 2022, **51**, 15496.
- 44 S. Kumari, A. Yadav, A. Kumari, S. Mahapatra, D. Kumar, J. Sharma, P. Yadav, D. Ghosh, A. Chakraborty and P. Kanoo, *Inorg. Chem.*, 2024, **63**, 7146.
- 45 J. E. Mondloch, M. J. Katz, W. C. Isley III, P. Ghosh, P. Liao, W. Bury, G. W. Wagner, M. G. Hall, J. B. DeCoste, G. W. Peterson, R. Q. Snurr, C. J. Cramer, J. T. Hupp and O. K. Farha, *Nat. Mater.*, 2015, **14**, 512.
- 46 S. Moon, E. Prousaloglou, G. W. Peterson, J. B. DeCoste, M. G. Hall, A. J. Howarth, J. T. Hupp and O. K. Farha, *Chem. – Eur. J.*, 2016, **22**, 14864.
- 47 Y. Liu, S.-Y. Moon, J. T. Hupp and O. K. Farha, *ACS Nano*, 2015, **9**, 12358.
- 48 Q.-L. Zhu and Q. Xu, *Chem. Soc. Rev.*, 2014, **43**, 5468.
- 49 S. Yadav, R. Dixit, S. Sharma, S. Dutta, K. Solanki and R. K. Sharma, *Mater. Adv.*, 2021, **2**, 2153.
- 50 R. Kumar, K. Jayaramulu, T. K. Maji and C. N. R. Rao, *Chem. Commun.*, 2013, **49**, 4947.
- 51 R. Kumar, K. Jayaramulu, T. K. Maji and C. N. R. Rao, *Dalton Trans.*, 2014, **43**, 7383.
- 52 G. Lu, O. K. Farha, L. E. Kreno, P. M. Schoenecker, K. S. Walton, R. P. Van Duyne and J. T. Hupp, *Adv. Mater.*, 2011, **23**, 4449.
- 53 R. Jena, S. Bhattacharyya, N. Bothra, V. Kashyap, S. K. Pati and T. K. Maji, *ACS Appl. Mater. Interfaces*, 2023, **15**, 27893.
- 54 S. Bhattacharyya, B. Konkena, K. Jayaramulu, W. Schuhmann and T. K. Maji, *J. Mater. Chem. A*, 2017, **5**, 13573.
- 55 A. Ghosh, S. Karmakar, F. A. Rahimi, R. S. Roy, S. Nath, U. K. Gautam and T. K. Maji, *ACS Appl. Mater. Interfaces*, 2022, **14**, 25220.
- 56 T. Mondal, D. Haldar, A. Ghosh, U. K. Ghorai and S. K. Saha, *New J. Chem.*, 2020, **44**, 55.
- 57 S. Zheng, Q. Li, H. Xue, H. Pang and Q. Xu, *Natl. Sci. Rev.*, 2020, **7**, 305.



- 58 B. Valizadeh, T. N. Nguyen, S. Kampouri, D. T. Sun, M. D. Mensi, K. Stylianou, B. Smit and W. L. Queen, *J. Mater. Chem. A*, 2020, **8**, 9629.
- 59 M. Zhao, K. Yuan, Y. Wang, G. Li, J. Guo, L. Gu, W. Hu, H. Zhao and Z. Tang, *Nature*, 2016, **539**, 76.
- 60 A. Alizadeh, S. Asghar, M. Roudgar-Amoli and Z. Shariatnia, *Process Saf. Environ. Prot.*, 2023, **177**, 507.
- 61 Y. Wang, Z. Zhang, M. Yang, J. Yuan, P. Li and M. Liu, *J. Colloid Interface Sci.*, 2022, **611**, 480.
- 62 D. Chen, M. Huang, S. He, S. He, L. Ding, Q. Wang, S. Yu and S. Miao, *Appl. Clay Sci.*, 2016, **119**, 109.
- 63 H. Zhao, H. Ye, J. Zhou, G. Tang, Z. Hou and H. Bai, *ACS Appl. Mater. Interfaces*, 2020, **12**, 49431.
- 64 D. Yang, Y. Li, L. Zhao, F. Cheng, L. Chang and D. Wu, *Chem. Eng. J.*, 2023, **466**, 143014.
- 65 F. Dai, J. Guo, Y. He, P. Song and R. Wang, *Clay Miner.*, 2021, **56**, 99.
- 66 S. Jafarnia, S. Sohrabnezhad and R. Foulady-Dehaghi, *J. Mol. Struct.*, 2023, **1289**, 135870.
- 67 H. Li, D. Meng, P. Qi, J. Sun, H. Li, X. Gu and S. Zhang, *Appl. Clay Sci.*, 2022, **216**, 106376.
- 68 R. R. Pawar, C. Chuaicham, K. Sekar, S. Rajendran and K. Sasaki, *Chemosphere*, 2022, **291**, 132922.
- 69 W. Gao, B. Mu, Y. Zhu and A. Wang, *Appl. Clay Sci.*, 2023, **242**, 107003.
- 70 S. Eslaminejad, R. Rahimi and M. Fayazi, *J. Taiwan Inst. Chem. Eng.*, 2023, **152**, 105181.
- 71 J. Xu, J. Gao, Y. Liu, Q. Li and L. Wang, *Mater. Res. Bull.*, 2017, **91**, 1.
- 72 Q. Jiang, Z. Han, N. Qu, L. Sun, Y. Yuan, Y. Ren and Z. Cheng, *Appl. Clay Sci.*, 2022, **218**, 106427.
- 73 I. A. Vasiliadou, T. Ioannidou, M. Anagnostopoulou, A. Polyzotou, D. Papoulis and K. C. Christoforidis, *Appl. Sci.*, 2022, **12**, 7468.
- 74 B. Hou and J. Wu, *Dalton Trans.*, 2020, **49**, 17621.
- 75 S. Li, H. Zhang, G. Wu, J. Wu and H. Hou, *Dalton Trans.*, 2023, **52**, 6899.
- 76 J. Deng, H. Zhao, T.-T. Zhang, F.-R. Kang and T.-B. Zhou, *J. Appl. Polym. Sci.*, 2023, **140**, 54517.
- 77 H. Liu, J. Chen, W. Yuan, C. Jiang, H. Li, J. Li, Y. Li, B. Zhang and Z. Chen, *J. Sol-Gel Sci. Technol.*, 2021, **99**, 55.
- 78 H. S. Far, M. Najafi, M. Hasanzadeh and R. Rahimi, *New J. Chem.*, 2022, **46**, 23351.
- 79 Q. Yu, J. Gong, W. Kong, Y. Long, J. Chen, L. Pu, H. Zhang and Y. Dai, *Electrochim. Acta*, 2022, **428**, 140913.
- 80 S. Wu, D. Cai, Z. Tian, L. Guo and Y. Wang, *J. Energy Storage*, 2024, **89**, 111670.
- 81 R. Soltani, A. Marjani and S. Shirazian, *Dalton Trans.*, 2020, **49**, 5323.
- 82 R. Soltani, R. Pelalak, M. Pishnamazi, A. Marjani, A. B. Albadarin, S. M. Sarkar and S. Shirazian, *Sci. Rep.*, 2021, **11**, 1609.
- 83 Y. Xie, G. Huang, J. Li, Q. Zhang, L. Fan and W. Liu, *Appl. Organomet. Chem.*, 2023, **37**, 7279.
- 84 H. Cai, K. Ma, Y. Zhang, X. Li, W. Wang and S. Tong, *Carbon Res.*, 2023, **2**, 23.
- 85 X. Hu, W. Zheng, M. Wu, L. Chen and S. Chen, *Sustainable Mater. Technol.*, 2023, **37**, 00691.
- 86 A. Chakraborty, P. Sutar, P. Yadav, M. Eswaramoorthy and T. K. Maji, *Inorg. Chem.*, 2018, **57**, 14480.
- 87 P. Sutar, V. R. Bakuru, P. Yadav, S. Laha, S. B. Kalidindi and T. K. Maji, *Chem. – Eur. J.*, 2021, **27**, 3268.
- 88 M. A. Browe, J. Landers, T. M. Tovar, J. J. Mahle, A. Balboa, W. O. Gordon, M. Fukuto and C. J. Karwacki, *ACS Appl. Mater. Interfaces*, 2021, **13**, 10500.
- 89 P. Zhang, J. Wang, Y. Jia, W. Li, X. Tan, D. Zhang, S. Xu, P. Zhang, C. Wei and S. Miao, *Appl. Clay Sci.*, 2019, **181**, 105226.
- 90 A. Chakraborty, A. Achari, M. Eswaramoorthy and T. K. Maji, *Chem. Commun.*, 2016, **52**, 11378.
- 91 A. Chakraborty, S. Roy, M. Eswaramoorthy and T. K. Maji, *J. Mater. Chem. A*, 2017, **5**, 8423.
- 92 A. Chakraborty, S. Laha, K. Kamali, C. Narayana, M. Eswaramoorthy and T. K. Maji, *Inorg. Chem.*, 2017, **56**, 9426.
- 93 S. Laha and T. K. Maji, *Adv. Funct. Mater.*, 2022, **32**, 2203093.
- 94 Jyoti, S. Kumari, S. Chakraborty, P. Kanoo, V. Kumar and A. Chakraborty, *Dalton Trans.*, 2024, **53**, 15815.
- 95 J. Imanipoor and M. Mohammadi, *Langmuir*, 2022, **38**, 5900.
- 96 Q. Cao, M. Huang, L. Qian, J. Wang, D. Wang and X. Zheng, *Dalton Trans.*, 2024, **53**, 2265.
- 97 L. T. N. Ngoc and Y.-C. Lee, *Sens. Actuators, A*, 2022, **344**, 113749.
- 98 M. Ding, R. W. Flaig, H.-L. Jiang and O. M. Yaghi, *Chem. Soc. Rev.*, 2019, **48**, 2783.
- 99 N. T. Whilton, S. L. Burkett and S. Mann, *J. Mater. Chem.*, 1998, **8**, 1927.
- 100 A. A. J. Ranchani, V. Parthasarathy, C. Hu, Y.-F. Lin, K.-L. Tung and R. Anbarasan, *Chem. Eng. Commun.*, 2020, **207**, 871.
- 101 K. Zheng, L. Liao, Y. Zhan, H. Tan, J. Liu, C. Li and D. Jia, *J. Colloid Interface Sci.*, 2022, **619**, 75.
- 102 Z. Li, S. Mao, Y. Yang, Z. Sun and R. Zhao, *J. Colloid Interface Sci.*, 2021, **585**, 85.
- 103 Y. Zhao, Z. Zhou, G. Chen and Q. Li, *J. Mater. Sci.: Mater. Electron.*, 2020, **31**, 6866.
- 104 G. Cai, M. Ding, Q. Wu and H. Jiang, *Natl. Sci. Rev.*, 2020, **7**, 37.
- 105 X. Zeng, Z. Cai, C. Zhang, D. Wang, J. Xu and X. Wang, *Mater. Res. Lett.*, 2022, **10**, 88.
- 106 G. Wang, D. Huang, M. Cheng, S. Chen, G. Zhang, L. Lei, Y. Chen, L. Du, R. Li and Y. Liu, *Coord. Chem. Rev.*, 2022, **460**, 214467.
- 107 N. Xie, X. Zhang, Y. Guo, R. Guo, Y. Wang, Z. Sun, H. Li, H. Jia, T. Jiang, J. Gao, J. Wang, D. Niu and H.-b. Sun, *J. Taiwan Inst. Chem. Eng.*, 2021, **127**, 197.
- 108 X. Liu, X. Sun, X. Sun, M. Shen, R. Liu, C. Yang and M. Fan, *Mater. Today Sustainability*, 2022, **17**, 100092.
- 109 R. Soltania, R. Pelalakb, M. Pishnamazib, A. Marjanie and S. Shiraziang, *Arabian J. Chem.*, 2021, **14**, 103052.

- 110 D. W. Thompson and J. T. Butterworth, *J. Colloid Interface Sci.*, 1992, **151**, 236.
- 111 Q. Wang, J. L. Mynar, M. Yoshida, E. Lee, M. Lee, K. Okuro, K. Kinbara and T. Aida, *Nature*, 2010, **463**, 339.
- 112 P. Sutar and T. K. Maji, *Chem. Commun.*, 2016, **52**, 8055.
- 113 P. Sutar, V. M. Suresh, K. Jayaramulu, A. Hazra and T. K. Maji, *Nat. Commun.*, 2018, **9**, 3587.
- 114 M. Tsotsalas, J. Liu, B. Tettmann, S. Grosjean, A. Shahnas, Z. Wang, C. Azucena, M. Addicoat, T. Heine, J. Lahann, J. Overhage, S. Bräse, H. Gliemann and C. Wöll, *J. Am. Chem. Soc.*, 2014, **136**, 8.
- 115 J.-R. Li, R. J. Kuppler and H.-C. Zhou, *Chem. Soc. Rev.*, 2009, **38**, 1477.
- 116 A. Schneemann, V. Bon, I. Schwedler, I. Senkovska, S. Kaskel and R. A. Fischer, *Chem. Soc. Rev.*, 2014, **43**, 6062.
- 117 K. S. Park, Z. Ni, A. P. Côté, J. Y. Choi, R. Huang, F. J. Uribe-Romo, H. K. Chae, M. O'Keeffe and O. M. Yaghi, *Proc. Natl. Acad. Sci. U. S. A.*, 2006, **103**, 10186.
- 118 H. R. Moon, D.-W. Limb and M. P. Suh, *Chem. Soc. Rev.*, 2013, **42**, 1807.